Bubble Growth Dynamics For C_3F_8 Bubble Chambers

by

Alexandre Le Blanc

A thesis submitted in partial fulfillment

of the requirements for the degree of

Master of Science (MSc.) in Physics

The Faculty of Graduate Studies

Laurentian University

Sudbury, Ontario, Canada

THESIS DEFENCE COMMITTEE/COMITÉ DE SOUTENANCE DE THÈSE
Laurentian Université/Université Laurentienne
Faculty of Graduate Studies/Faculté des études supérieures

Title of Thesis
Titre de la thèse — Bubble Growth Dynamics For C_3F_8 Bubble Chambers

Name of Candidate
Nom du candidat — Leblanc, Alexandre

Degree
Diplôme — Master of Science

Department/Program
Département/Programme — Physics

Date of Defence
Date de la soutenance — April 12, 2019

APPROVED/APPROUVÉ

Thesis Examiners/Examinateurs de thèse:

Dr. Ubi Wichoski
(Supervisor/Co-directeur de thèse)

Dr. Ian Lawson
(Co-Supervisor/Co-directeur de thèse)

Dr. Rizwan Haq
(Committee member/Membre du comité)

Dr. Jacques Farine
(Committee member/Membre du comité)

Dr. Gilles Gerbier
(External Examiner/Examinateur externe)

Approved for the Faculty of Graduate Studies
Approuvé pour la Faculté des études supérieures
Dr. David Lesbarrères
Monsieur David Lesbarrères
Dean, Faculty of Graduate Studies
Doyen, Faculté des études supérieures

ACCESSIBILITY CLAUSE AND PERMISSION TO USE

Abstract

PICO is a direct dark matter search experiment that utilizes bubble chambers and the acoustics of growing bubbles to discriminate signal from background events [5]. It has been shown that temperature perturbations from equilibrium significantly affect the growth of a bubble in superheated water [17], particularly in the form of an onset delay to perceptible growth. In this thesis the temperature perturbation method is applied to superheated C_3F_8 to describe the acoustic background discrimination achieved by the PICO experiment. We reproduced the delay in water and confirmed its occurrence in C_3F_8. We hypothesized that the delay can be used for optical background discrimination. However, it was shown that the model does not apply to the energy deposition of different types of particles as all of them, e.g. incoming alpha particles and neutron induced nuclear recoils, create multiple bubbles along their tracks. Those bubbles, in the end, coalesce to form the observed single visible bubble.

Acknowledgments

So many people deserve to be listed here and I will do my best to honor them all. I believe that everyone who has kept my mind and body healthy should be on this list. Of course, I would like to thank both my supervisors Ubi Wichoski and Ian Lawson who were an important part of my success and they never gave up on me. Alexander Robillard, the greatest of friends, deserves my greatest thanks as he was the ”goto” for idea bouncing and theorycrafting and without whom my knowledge would not have progressed to where it is now. The next group of people: Jamie Grove, Alexus McCue, Michael Blouin and Ali Weslake deserve all the praise of keeping me at the highest level of physical training and supporting me through my injuries. I would like to thank my officemates, Olivia Scallon, Frédéric Girard, Tristan Hillier, Anthony Demesrobian (close enough to my office), Esther Weima and Michel Lapointe (during his short stay in the office) for all the support they have given me and time we spent together. Finally, I would like to thank my close friends Ralitsa Sharankova, Danika Mercier and Mélodie Cyr for always being there for me in time of need.

Contents

List of Figures

Preface

Around 1937, Swiss astronomer Franz Zwicky was working on the problem of determining the mass of a galaxy. He stated that the mass of a galaxy could not be determined by its luminosity and internal rotation alone [1][2]. Even when taking into consideration the movement of clusters of galaxies using the virial theorem to infer the mass of a galaxy, they would still differ by large factors [1]. In the early 1970's, Vera Rubin measured the angular velocities of stars within Andromeda [3][4]. The measured velocities could not be explained by Newtonian mechanics. Both Zwicky's and Rubin's observations may be explained with the presence of mass that is invisible. This has led the scientific community to search for different solutions outside the standard model of particle physics which describes all known fundamental particles and their interactions. There are generally two extremes: either the model is incomplete or incorrect. The thesis will focus on the former, where completing the model by adding a new particle is the simplest solution. The most widely accepted solution involves the addition of a dark matter particle called the Weakly Interacting Massive Particle (WIMP). There are many experiments actively trying to search for the WIMP.

PICO is one of the many direct dark matter search experiments. PICO utilizes the principle of a

bubble chamber, where a phase transition is triggered by the energy transfer from the scattering of the dark matter particle with standard matter. The phase transition, under the right circumstances, will cause a bubble to grow and create an audible acoustic wave. Both the acoustic wave and the presence of a bubble can be observed.

The problem with detecting the dark matter particle is twofold: the scattering interaction cross section is very small and the dark matter signal in an experiment is buried by other signals called backgrounds. For example, in PICO, these other signals are bubbles caused by neutrons, alphas, photons, etc. All experiments study their backgrounds extensively and attempt to reduce those signals, potentially allowing the detection of the dark matter signal. It was observed in PICASSO, one of the two collaboration that merged to form PICO, that bubbles caused by alpha particles are louder than bubbles caused by neutrons or other nuclear recoils. PICO developed a tool called the Acoustic Parameter (AP) that quantitatively assesses this phenomenology and provides powerful differentiation between alpha particle events and nuclear recoil events [5].

Outside the field of particle physics, it was shown numerically that a bubble initially at equilibrium in a superheated liquid can grow if the initial conditions are perturbed [17][19]. The perturbation can be in size, vapor pressure, vapor temperature, etc. One of the results showed that the magnitude of the perturbation affected the growth of the bubble significantly. If a relation exists between the initial conditions of a bubble and the energy deposition of a particle along a track, this would provide a new tool to discriminate particles with their associated bubble growth. This is the premise of the present thesis.

Chapter 1

Dark Matter

At this moment, only the effects of dark matter have been observed. These observations were first made by Franz Zwicky [1][2] and Vera Rubin [3] but other more contemporary groups have also made observations that corroborate the existence of dark matter. In the following sections, the two observations of Zwicky and Rubin will be examined to put forth the first evidence of dark matter at the scales of clusters of galaxies.

1.1 Luminous Mass Discrepancy

This section will closely follow the articles written by Zwicky: *On The Masses of Nebulae and of Clusters of Nebulae* [1] and *On The Red Shift of Spectral Lines Through Interstellar Space* [2]. In 1937, Swiss astronomer Fritz Zwicky was working on the problem of estimating the mass of galaxies. At that time, the mass of galaxies was based upon luminosities and internal rotations.

However, as will be reported, Zwicky argued that estimating masses of galaxies from absolute luminosities is dubious and using internal rotations alone cannot yield the mass of a galaxy. In order to help with the problem, Zwicky developed several tools to estimate the mass of galaxies, one of which was to apply the virial theorem to a cluster of galaxies. Doing so, Zwicky calculated the ratio of the total mass of the cluster from his method to the luminous mass of the cluster and it was much greater than one. Even though his method was inaccurate, it showed correctly that these galaxies were much more massive than what was observed, providing the evidence for the existence of dark matter.

1.1.1 Mass-luminosity Relation of a Galaxy

The observed luminosity of a star is a good approximation of its *mass* through the relation $L \approx CM^{3.5}$, where L is the luminosity, C is a constant and M is the mass of the star. This particular relation is only accurate for stars along the main sequence as other stars would have different factors and exponents. Therefore, for the formula to be used for a galaxy, one would require details of the proportions of the various stars that compose the galaxy. The absolute luminosity of an object is measured from its black-body radiation. In the case of a galaxy, it will contain gases, dust, planets, dwarf stars and any other cold non-radiating mass that may absorb some radiation and affect the luminosity measurement. This would lead to having only surface information about the galaxy. At that time, Zwicky had very limited, or nonexistent, information about the composition of the galaxies he was observing. Luminosity, therefore, can only furnish the lowest of limits of the mass of a galaxy.

1.1.2 Mass From Internal Rotation

There are several models of galaxy dynamics. In some simplified models, analyzing the mechanics of the system can give an estimate of the total mass. Two limiting models for galaxies are discussed in this section, one whose internal viscosity is negligible and the other whose internal viscosity is very large. This will show the difficulties faced by astronomers when trying to determine the mass of a galaxy.

Model Galaxy With Negligible Internal Viscosity

A model galaxy with negligible internal viscosity can be described by a heavy small nucleus of mass, M_0, with a given number of stars, n, of average mass, $M_s << M_0/n$, orbiting outside the nucleus. The mutual gravitational interaction between these orbiting stars is negligible, and therefore the system is said to have an internal viscosity of zero. For such a system, it is possible to distribute the n stars' orbits in such a way that the average angular velocity of the system, S_0, is zero in every point. In this theoretical construct, due to the orbits being non-interacting, any number of stellar orbits may be reversed. In this way, the specified distribution of average angular velocities of this new system, S, may be constructed where the remaining characteristics such as mass, luminosity and shape remain unchanged. Thus, the observed angular velocities give no indication of the mass of a galaxy.

Model Galaxy With Large Internal Viscosity

This model is built up of stars, dust and gases in such a fashion that the gravitational interactions between the various components as well as collisions influence the path of all mass components. Many changes in energy and momentum of the components will occur in time scales that are shorter than the average orbital period of a mass component of the same initial velocity. This model is analogous to elementary particles moving inside a star. This model of a galaxy will therefore rotate as a solid body, regardless of what its total mass and its distribution of mass over different regions of the system may be. The conclusion that was usually put forward is that constant angular velocity necessarily implies a uniform distribution of mass, which is erroneous.

Actual Galaxies

Actual galaxies have aspects of both limiting cases. They are composed of a central highly viscous core whose relative dimensions are not negligible but of comparable size with the extension of the whole system. Outside the core are negligibly interacting components. The core would rotate as a solid body and thus have constant angular velocity whilst the outlying distribution of angular velocities can be arbitrary depending on the falloff of the viscosity. From the distribution of the outlying masses it would seem that the outliers of many galaxies were at some point part of the core but were ejected. In that case, assuming that these outliers only interact gravitationally with the core and the interactions amongst themselves may be neglected, the angular velocities would decrease as $1/\sqrt{r}$. Fortunately, there are three additional models to derive the mass of a galaxy proposed by Zwicky but only one model is important for the evidence of dark matter. Zwicky

proposed to apply the virial theorem to clusters of galaxies. By doing so, the mass of galaxies will differ from their luminous mass by non-negligible factors.

1.1.3 Mass of Galaxies From Applying the Virial Theorem to a Cluster of Galaxies

Under the assumption that clusters of galaxies, such as the coma cluster represented in figure 1.1 are mechanically stationary systems, the virial theorem gives the total mass of the cluster in terms of the average square of the velocities of the individual galaxies that constitute the cluster.

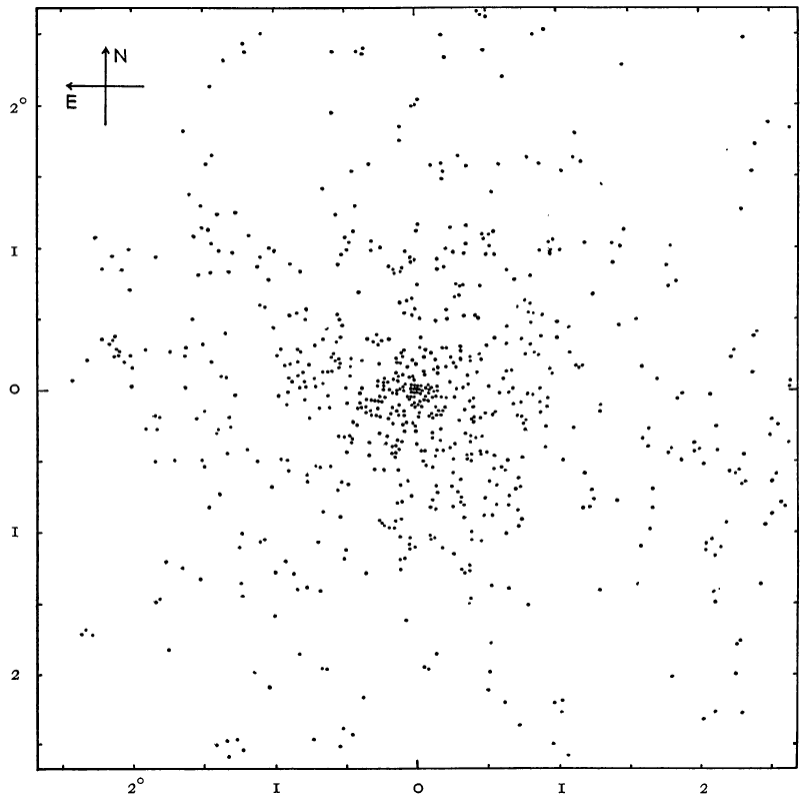

Figure 1.1: Coma cluster representation, black dots are galaxies [1].

Even without the cluster being stationary, with additional data, it is still possible to draw important

conclusions concerning the mass of the cluster. Suppose that the radius vector from a point inside the cluster to a galaxy, denoted by subscript i, of mass, M_i, is $\vec{r}_i$. Choosing the center of mass of the cluster for the origin makes the calculations easier. The fundamental law of motion for this galaxy is

$$M_i \frac{d^2\vec{r}_i}{dt^2} = \vec{F}_i \ . \tag{1.1}$$

Scalar multiplication with respect to $\vec{r}_i$ and summation over all galaxies gives

$$\sum_i \frac{1}{2}\frac{d^2}{dt^2}\left(M_i \vec{r_i^2}\right) = \sum_i \vec{F}_i \cdot \vec{r}_i + \sum_\sigma M_i \left(\frac{d\vec{r}_i}{dt}\right)^2, \tag{1.2}$$

for terminology, from left to right, the first term inside the derivative is the polar moment of inertia of the cluster, Θ, the second term is the virial of the cluster, Vir, and the third term is two times the sum of the kinetic energies, K_T of the individual galaxies, thus equation 1.2 reduces to

$$\frac{1}{2}\frac{d^2\Theta}{dt^2} = Vir + 2K_T \ . \tag{1.3}$$

If the cluster is stationary, the polar moment of inertia will oscillate around a constant value, therefore the time average of its derivatives with respect to time will be zero. Denoting time averages with overbar notation, equation 1.3 reduces to

$$\overline{Vir} = -2\overline{K_t} \ . \tag{1.4}$$

It is worthwhile to expand the virial, the overbar will be dropped and taken care of at the end,

giving

$$Vir = \sum_{i=1}^{N} \vec{F}_i \cdot \vec{r}_i \ , \tag{1.5}$$

whereas the force $\vec{F}_i$ is the total force acting on mass i, therefore $\vec{F}_i = \sum_{j=1}^{N} \vec{F}_{ji}$. Also since $\vec{F}_{ji} = -\vec{F}_{ij}$ it is possible to write

$$Vir = \sum_{i=2}^{N} \sum_{j=1}^{i-1} \vec{F}_{ji} \cdot (\vec{r}_i - \vec{r}_j) \ . \tag{1.6}$$

If the forces acting on the galaxies are conservative, the forces can be described in terms of the gradient of a potential, $\Phi(r)$, giving

$$\vec{F}_{ji} = -\vec{\nabla}\Phi \ , \tag{1.7}$$

$$\vec{F}_{ji} = \frac{\partial \Phi}{\partial r} \left(\frac{\vec{r}_i - \vec{r}_j}{r_{ji}} \right) \ , \tag{1.8}$$

and the virial would become

$$Vir = \sum_{i=2}^{N} \sum_{j=1}^{i-1} \frac{\partial \Phi}{\partial r} \frac{|\vec{r}_i - \vec{r}_j|^2}{r_{ji}} \ , \tag{1.9}$$

$$Vir = \sum_{i=2}^{N} \sum_{j=1}^{i-1} \frac{\partial \Phi}{\partial r} r_{ji} \ . \tag{1.10}$$

In the case of gravitational potential, $\Phi(r_{ji}) = -Gm_j m_i / r_{ji}$, and the virial is

$$Vir = \sum_{i=2}^{N} \sum_{j=1}^{i-1} \frac{Gm_j m_i}{r_{ji}^2} r_{ji} \ , \tag{1.11}$$

$$Vir = \sum_{i=2}^{N} \sum_{j=1}^{i-1} \frac{Gm_j m_i}{r_{ji}} \ . \tag{1.12}$$

The virial in the case of gravitating galaxies is just the total gravitational potential energy. Zwicky

follows by approximating the point-mass distribution to a uniform and continuous distribution of mass, such that each galaxy can be described as an element of mass, $m_i = dm = \rho(r)d^3r$. In this case, the gravitational potential would be written as

$$\Phi(r) = -2\pi G \int_0^{\pi} \int_0^{\infty} \frac{\rho(r',\theta)}{|\vec{r'} - \vec{r}|} r'^2 dr' d\theta \ , \tag{1.13}$$

assuming an axially symmetric potential. Using the Laplace expansion for $|r - r'|^{-1}$

$$|r - r'|^{-1} = \sum_{l=0}^{\infty} \left(\frac{r'}{r} P_l(cos\theta) \right) \ , \tag{1.14}$$

the potential becomes

$$\begin{aligned} \Phi(r) = -\frac{2\pi G}{(n+1/2)\, r^{n+1}} \int_0^r \int_0^{\pi} r'^{n+2} (n+1/2) P_n(cos\theta) \rho(r',\theta) dr' sin(\theta) d\theta \\ - 2\pi G r^n \int_r^{\infty} \int_0^{\pi} r'^{1-n} (n+1/2) P_n(cos\theta) \rho(r',\theta) dr' sin(\theta) d\theta \ , \end{aligned} \tag{1.15}$$

which can be simplified by describing the density with Legendre Polynomials as

$$\rho(r,\theta) = \sum_n^{\infty} \rho(r) P_n(cos\theta) \tag{1.16}$$

$$\rho_n(r) = (n+1/2) \int_n^{\pi} \rho(r,\theta) P_n(cos\theta)\, sin\theta d\theta \tag{1.17}$$

$$\Phi_n(r) = -\frac{2\pi G}{n+1/2} r^{n+1} \int_0^r r'^{n+2} \rho_n(r') dr' - \frac{2\pi G r^n}{n+1/2} \int_r^{\infty} r'^{1-n} \rho_n(r') dr' \ , \tag{1.18}$$

if the density is a constant, $\rho(r,\theta) = \rho$, until $r = R$ and vanishes for $r > R$, only P_0 contributes and $P_{n>0} = 0$ and the problem is independent of both r and θ, thus the problem is equivalent to a

spherically symmetric problem. For $r \leq R$, the potential would be

$$\Phi(r) = \Phi_0(r) = -\frac{4\pi G\rho}{r}\int_0^r r'^2 dr' - 4\pi G\rho \int_r^R r' dr \; . \tag{1.19}$$

For $r > R$ the potential becomes

$$\Phi(r) = \Phi_0(r) = -\frac{4\pi G\rho}{r}\int_0^R r'^2 dr' \; . \tag{1.20}$$

When calculating the gravitational potential energy at r for the case of a constant mass density, only the mass at positions $r' \leq r$ will contribute. Thus the gravitational potential energy of a system that extends until $r = R$ is

$$E_p = \int_0^R -G\frac{\left(\frac{4}{3}\pi\rho r^3\right)\left(4\pi\rho r^2\right)}{r} dr \tag{1.21}$$

$$E_p = -\frac{3GM^2}{5R} \; , \tag{1.22}$$

which is a well known result of classical mechanics. The virial is now expressed as the total mass of cluster M. The time averaged kinetic energy can be directly related to the total mass and the average velocity squared

$$\sum_i M_i \overline{v_i^2} = M\overline{\overline{v^2}} \; , \tag{1.23}$$

where the double overbar indicates averages over time and masses. Equations 1.4, 1.22, 1.23 can be combined to give

$$M = \frac{5R\overline{\overline{v^2}}}{3G} \; . \tag{1.24}$$

Since figure 1.1 is a two-dimensional image, it is unclear that the galaxies are uniformly distributed in space. In fact, the galaxies seem denser in the center. Although, grouping the mass in a sphere of radius R/n would increase the potential energy by only a factor of n. The value of the potential energy can only change slightly if it is assumed that the M_σ's run through a wide range. Zwicky provides an example where the mass of the cluster is dominated by two or three galaxies of mass $M/2$ or $M/3$ whose mutual distances are as small as $R/10$. The total potential energy of the cluster for these two examples would be

$$E_{p,1} = \frac{-G\left(\frac{M}{2}\right)^2}{\frac{R}{10}} = \frac{-\frac{10}{4}GM^2}{R} \,, \tag{1.25}$$

$$E_{p,2} = \frac{-G\left(\frac{M}{3}\right)^2}{\frac{R}{10}} = \frac{-\frac{10}{9}GM^2}{R} \,, \tag{1.26}$$

where energies are of the same order of magnitude. Only the projection of the velocity along the line of sight of the observer is known. This has the effect of turning equation 1.24 into an inequality,

$$M > \frac{5R\overline{\overline{v_{obs}^2}}}{3G} \,, \tag{1.27}$$

where v_{obs} is the observed velocity, i.e. the projection. Similarly to the previous problem, the total mass is correct in orders of magnitude.

Since the number of galaxies within the coma cluster is known, it is possible to compare the average galactic mass to the luminous mass. The factor that Zwicky calculated is 500 for the Coma cluster. The average mass of the Coma cluster was 500 times the mass from the luminosity; this result is used as evidence for invisible mass, or what is currently termed dark matter. On a side note, Zwicky follows by presenting the factor calculated for the Kapteyn cluster which is only a factor

of 3 which is within his expected values. Zwicky follows in the remaining of his article by trying to add additional terms to correct these ratios but both ratios are still greater than 1. The important conclusion is that ratios greater than 1, even with correction factors, point to invisible missing mass affecting the kinematics of clusters of galaxies.

1.2 Stellar Angular Velocity Discrepancy

This section will closely follow the articles of Vera Rubin: *Rotation of Andromeda Nebula From a Spectroscopic Survey of Emission Regions* [3] and *A Note on the Systemic Velocity of M 31* [4]. In the early 1970's, Vera Rubin and others were attempting to characterize Andromeda. She measured the angular velocities of stars within the galaxy using primarily H_α spectral lines. As seen in figure 1.2, the galaxy appears to be elliptic in shape, but in fact it is a rotated circle in three dimensions. Additionally, the galaxy itself is moving in some direction. At this scale, all measurements are done with wavelength shifts of spectral lines. One characteristic of such measurements is that they are the projection of the true velocity onto the line of sight of the observer. This leads to varying errors depending on location of the observed star because of the dependence on the chosen rotation angles. Nonetheless, all rotation angles of Andromeda's galactic plane have been measured by Vera Rubin and others. In the end, she observed that the angular velocities of the stars did not drop off as the distance from the center increased as expected by classical mechanics but instead it plateaued. The following is a brief review of her measurements.

1.2.1 Galactic Characterization

An image of the Andromeda galaxy is shown in figure 1.2. It is accepted that Andromeda is a circular spiral disk galaxy. H. Arp gives the following definition of a spiral galaxy: "[a galaxy] is called spiral if its outer parts are in the form of luminous tubes coiled more or less around the center in a spiral pattern" [6]. A spiral is defined in the dictionary as a continuous and gradually widening curve. From these definitions, Vera Rubin's image of the Andromeda galaxy [4] and additional data from Arp [6], some material, dust or gas, may be identified to be spiraling towards the nucleus. Andromeda, as seen in the image, appears elliptical and, additionally, the apparent semi-minor and semi-major axes are rotated with respect to the standard axes. One of the main difficulties is measuring the rotation angles of Andromeda, mainly the rotation with respect to the apparent semi-major axis which leads Andromeda to appear elliptical. That angle has the largest effect on the orbital velocities that Vera Rubin presents [4][6]. For this reason, it is important to investigate the transformation of a circular disk to an elliptical disk of the same shape as Andromeda to understand the effects of the two angles will have on the data.

The process that will be described here is the reverse of figure 1.3. A circle will be parametrized in the XYZ space and a set of axes X', Y' and Z' will be attached to the circle. The circle will be rotated with respect to the Z axis; this will align the Y' axis with the apparent semi-major axis of the Andromeda image. Finally, a rotation with respect to the Y' axis will match the X' axis with the apparent semi-minor axis and it will give the circle the appearance of an ellipse in the XY plane. Mathematically, starting with a parametrized circle in three dimensions in the standard

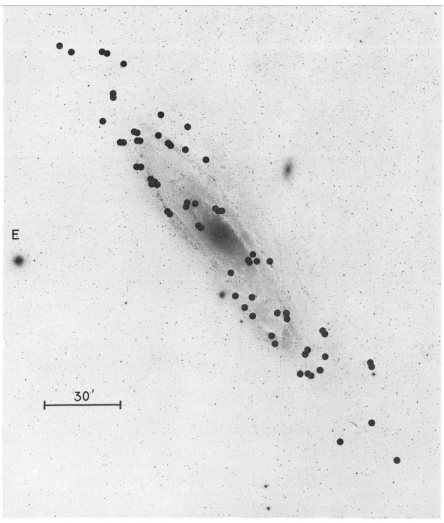

Figure 1.2: Image of Andromeda taken by Vera Rubin with identification chart for emission regions [3].

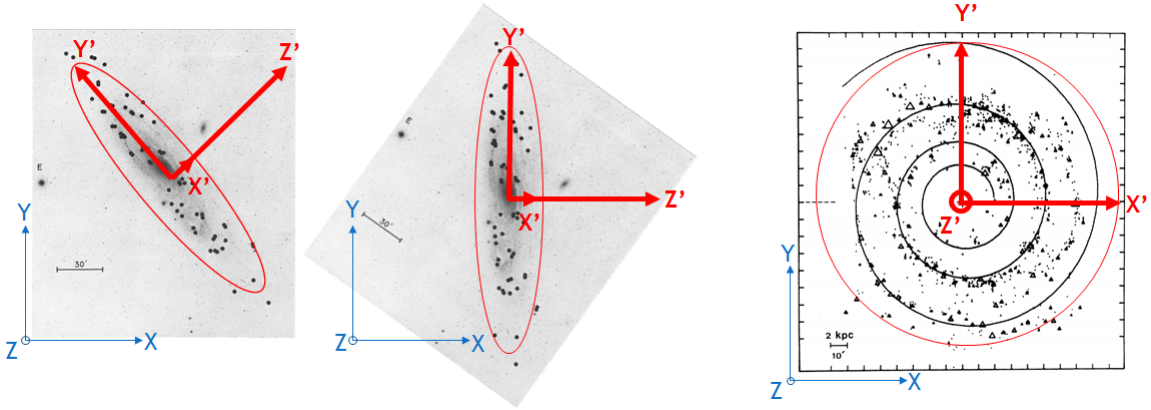

Figure 1.3: Depiction of the process to align Andromeda's galactic plane axes with the standard axes. Many methods exist to circularise the image. Images are based on [3][6].

XYZ space

$$\vec{P}(t) = rcos(\omega t)\hat{e}_i + rsin(\omega t)\hat{e}_j + 0\hat{e}_k + \vec{C}\,, \tag{1.28}$$

$$\vec{P}(t) = \begin{bmatrix} rcos(\omega t) \\ rsin(\omega t) \\ 0 \end{bmatrix} + \vec{C}\,, \tag{1.29}$$

where $\vec{P(t)}$ is the position vector along the circle as a function of a parameter t, r is the radius

of the circle, $\hat{e}_{i,j,k}$ are the standard unit vectors of three dimensional space associated with the X, Y, Z axes, respectively, and $\vec{C}$ is the position of the center of the circle; N.B. the position vector of the center of the circle will be omitted as the rest only applies to the circle itself. From figure 1.3, and following the standard notation where the axis and the unit vector representing the axis have different names, the following will be used: $\hat{e}_u$ will be associated to the X' axis, $\hat{e}_v$ will be associated to the Y' axis and $\hat{e}_w$ will be associated to the Z' axis. The first rotation with respect to the Z axis aligns the Y' axis and the apparent semi-major axes of Andromeda. With the standard rotation matrices,

$$R_x(\theta) = \begin{bmatrix} 1 & 0 & 0 \\ 0 & cos(\theta) & -sin(\theta) \\ 0 & sin(\theta) & cos(\theta) \end{bmatrix}, \tag{1.30}$$

$$R_y(\theta) = \begin{bmatrix} cos(\theta) & 0 & sin(\theta) \\ 0 & 1 & 0 \\ -sin(\theta) & 0 & cos(\theta) \end{bmatrix} \text{ and} \tag{1.31}$$

$$R_z(\theta) = \begin{bmatrix} cos(\theta) & -sin(\theta) & 0 \\ sin(\theta) & cos(\theta) & 0 \\ 0 & 0 & 1 \end{bmatrix}, \tag{1.32}$$

the first rotation would be written as

$$R_z(\theta)\vec{P}(t) = \begin{bmatrix} cos(\theta) & -sin(\theta) & 0 \\ sin(\theta) & cos(\theta) & 0 \\ 0 & 0 & 1 \end{bmatrix} \begin{bmatrix} rcos(\omega t) \\ rsin(\omega t) \\ 0 \end{bmatrix} \tag{1.33}$$

$$R_z(\theta)\vec{P}(t) = \begin{bmatrix} rcos(\omega t)cos(\theta) - rsin(\omega t)sin(\theta) \\ rcos(\omega t)sin(\theta) + rsin(\omega t)cos(\theta) \\ 0 \end{bmatrix} . \tag{1.34}$$

The unit vectors that describe the set of axes X' and Y' can be written in terms of $\hat{e}_i$ and $\hat{e}_j$ as

$$\hat{e}_u = cos(\theta)\hat{e}_i + sin(\theta)\hat{e}_j \text{ and} \tag{1.35}$$

$$\hat{e}_v = -sin(\theta)\hat{e}_x + cos(\theta)\hat{e}_y . \tag{1.36}$$

The Y' axis, as previously stated, is aligned with the apparent semi-major axis of the Adromeda image 1.2. The circle can be described with a set of base vectors

$$\vec{P}(t) = rcos(\omega t)\hat{e}_u + rsin(\omega t)\hat{e}_v + 0\hat{e}_w + \vec{C}. \tag{1.37}$$

The second rotation is performed with respect to the Y' axis to give,

$$R_{Y'}(\phi)\vec{P}(t) = \begin{bmatrix} cos(\phi) & 0 & sin(\phi) \\ 0 & 1 & 0 \\ -sin(\phi) & 0 & cos(\phi) \end{bmatrix} \begin{bmatrix} rcos(\omega t) \\ rsin(\omega t) \\ 0 \end{bmatrix} = \begin{bmatrix} rcos(\omega t)cos(\phi) \\ rsin(\omega t) \\ -rcos(\omega t)sin(\phi) \end{bmatrix}, \tag{1.38}$$

$$\vec{P}(t) = rcos(\omega t)cos(\phi)\hat{e}_u + rsin(\omega t)\hat{e}_v - rcos(\omega t)sin(\phi)\hat{e}_w \ . \tag{1.39}$$

The parametrization is complete, the Y' axis is aligned with the apparent semi-major axis and the X' axis matches the apparent semi-minor axis. From Earth, only the projection of the velocities of stars onto the line of sight of the observer are measured. The results Vera Rubin presented are circular orbital velocities, therefore the velocities of the stars that she measured must be de-projected. This requires measuring the two angles. The method used by S. Simien [7] is in essence trial and error, assuming θ can be accurately and precisely measured, then various angles for ϕ can be tested and in theory only one angle would correctly de-project into circles. Another difficulty arises: Andromeda is a spiral and stars are continuously approaching the nucleus in a spiral pattern such as in figure 1.4. Usually the spiral structure is described by a function of the form $r = r_0 e^{k\theta}$, where $\theta = \omega t$ to be consistent with the previous notation. Simien still uses the same method to determine the angle ϕ but with a minor change. By plotting $(log(r), \omega t)$ the correct angle ϕ would lead to a straight line. However, if ϕ is too large, W-structures will be observed and if ϕ is too small M-structures will be observed. Simien presents the effect of ϕ in figure 1.5 [7]. A theoretical example is shown in figure 1.6 where an exact spiral structure is de-projected in various cases. Together these plots show that there is no satisfactory angle that perfectly circularizes the Andromeda image and that ϕ does not affect the apparent semi-major axis. Also, the various clusters in figure 1.5 most likely show that Andromeda is not a perfectly flat disk nor a perfect spiral.

There is the added problem if θ is incorrect, the location of the apparent semi-major and semi-minor axes is incorrect, no de-projection angle would yield straight lines because that scenario would be de-projecting an ellipse into another ellipse. Orbital velocities can be calculated by

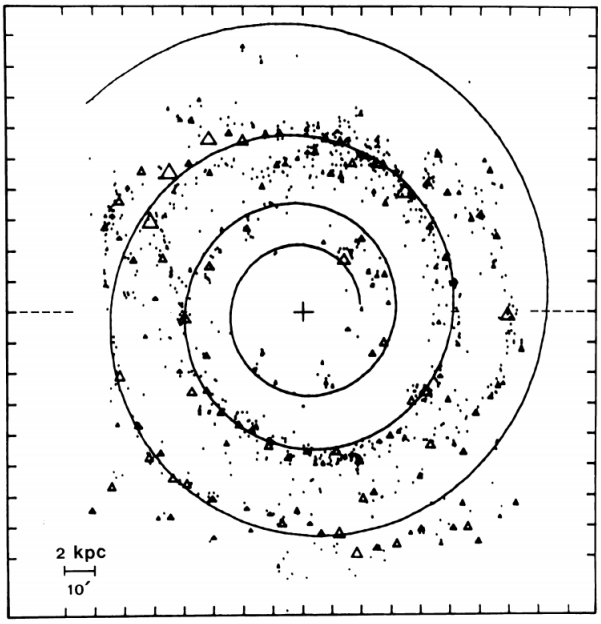

Figure 1.4: Andromeda view in a possible orbital plane [7].

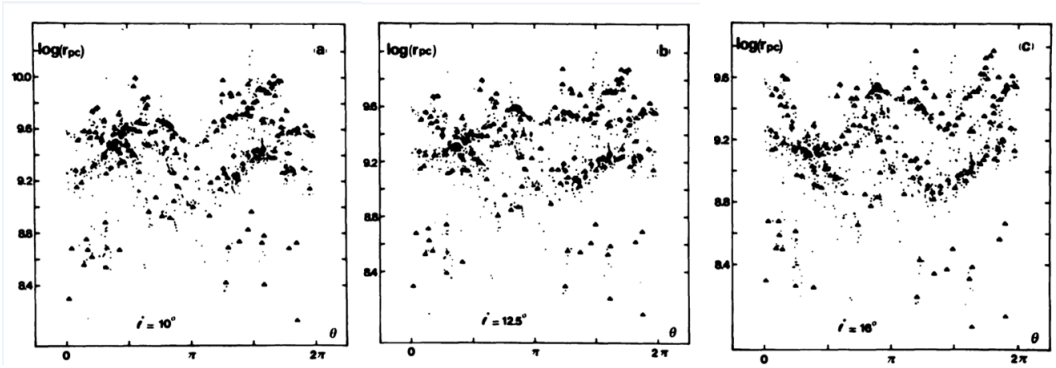

Figure 1.5: Example de-projection process of the Andromeda galaxy [7].

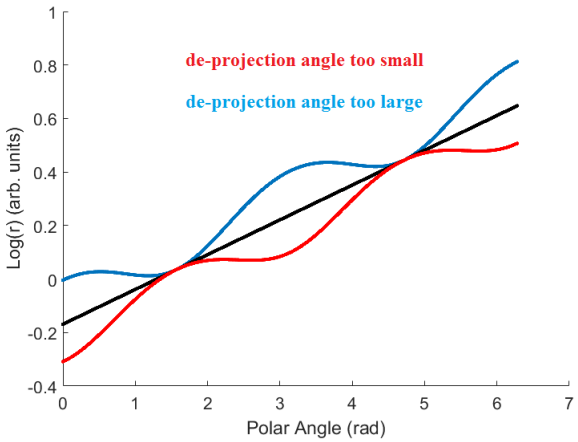

Figure 1.6: Theoretical example of de-projecting a spiral.

taking the derivative with respect to time of the position, from equation 1.39 this would yield the following

$$\frac{d\vec{P}(t)}{dt} = -r\omega sin(\omega t)cos(\phi)\hat{e}_u + r\omega cos(\omega t)\hat{e}_v + r\omega sin(\omega t)sin(\phi)\hat{e}_w + \dot{r}cos(\omega t)cos(\phi)\hat{e}_u + \dot{r}sin(\omega t)\hat{e}_v - \dot{r}cos(\omega t)sin(\phi)\hat{e}_w + \vec{V}_C \ , \quad (1.40)$$

where $\vec{V}_C$ is the velocity of the center of the circle. The projected velocities onto our line of sight cause a Doppler shift of spectral lines which can be measured from a spectrograph using a reference spectrum. Assuming the line of sight is the Z axis, the projection would be

$$\frac{d\vec{P}(t)}{dt} \cdot \hat{e}_k = r\omega sin(\omega t)sin(\phi) - \dot{r}cos(\omega t)sin(\phi) + \vec{V}_C \cdot \hat{e}_k. \quad (1.41)$$

The notation of Vera Rubin is obtained by using the following variables,

$$rsin(\omega t) = Y' \ , \quad (1.42)$$

$$rcos(\omega t)cos(\phi) = X' \ , \quad (1.43)$$

and renaming the following,

$$V_{rot} = r\omega \ , \quad (1.44)$$

$$E = \dot{r} \ , \quad (1.45)$$

$$\frac{d\vec{P}(t)}{dt} \cdot \hat{e}_k = V_{obs} \ , \quad (1.46)$$

$$\vec{V}_C \cdot \hat{e}_k = V_{center} \ . \quad (1.47)$$

This leads to the following equation,

$$V_{obs} - V_{center} = V_{rot} sin(\phi)\frac{Y'}{r} - E sin(\phi) sec(\phi)\frac{X'}{r} \ . \tag{1.48}$$

Vera Rubin states that there are no radial components to the velocities, i.e. they are non-expanding which implies $E = 0$. Andromeda being a spiral galaxy implies that the orbits must have radial components to reach the nucleus. Maybe her intent was to say $V_{rot} >> E$, therefore radial components may be neglected, giving

$$V_{obs} - V_c = V_{rot} sin(\phi)\frac{Y'}{r} \ , \tag{1.49}$$

where, on a final note, $r = \sqrt{X'^2 + Y'^2 sec^2(\phi)}$.

1.2.2 Vera Rubin's Results

This section will describe the process of measuring the position and angular velocities of objects within Andromeda. At these distance scales, only the nucleus can be resolved even though it is composed of many stars. Dust and gas are also visible due to their interaction with light and gives information of the morphology of the galaxy. The telescope Vera Rubin used was equipped with a slit whose width corresponded to 1.4 arcseconds of resolution on the sky. With this resolution, objects of 3.34 parsecs of diameter can be resolved. Vera Rubin did not visually resolve individual stars but instead measured the emission spectra of regions of Andromeda that may contain a star. She searched for specific emission lines that corresponded to a specific type of stars. A light source with velocity $\vec{V}$ will have its photon's wavelength shifted proportional to the component of

the source's velocity projected along the path of the photon. This relation can be expressed with a factor called z,

$$z = \frac{\lambda_{obs} - \lambda_e}{\lambda_e} \,, \tag{1.50}$$

$$z = \frac{v}{c} \,, \tag{1.51}$$

where v is the velocity of the source projected in the direction of the photon, λ_{obs} is the observed wavelength and λ_e is the emitted photon's wavelength. Stars within galaxies will have orbital velocities of hundred of kilometers per second, therefore the projection of the orbital velocity onto the line of sight of a detector, which also correspond to the path of the photon will cause a wavelength shift. These orbital velocities are fast enough to have noticeable shifts in wavelength when observing spectral rays of certain elements emitted by the stars. There are still several effects that may not be accounted for in Vera Rubin's models, for example, the Earth has its own spin and orbit, the Sun orbits our Galaxy and our Galaxy is also moving, all of which can affect the measured Doppler shifts.

Vera Rubin used an angle of 77° and $-300 \pm 5\ km/s$ for V_c presented in equation 1.49, which were obtained from various groups as decribed in reference [3]. Even though these value are not from her measurements, she used values determined by various groups [3]. Vera Rubin mentions that others have pointed out that certain parts of Andromeda appear to have different de-projection angles. Since Andromeda is not a perfectly flat disk, varying de-projection angles may be correct. Nonetheless, she used a constant value for all the data. Her results showed that the angular velocities do not drop off as would be described by using Keplerian mechanics to calculate the

orbital velocities of stars around a nucleus, but instead they plateau with increasing distance from the nucleus. This plateau leads to the conclusion that the mass of the galaxy must increase with increasing distance from the center of the galaxy as presented in figures 1.7 and 1.8. The luminosity of the galaxy decreases with distance from the center of the galaxy. This is what leads us to believe that there is a large amount of mass surrounding the galaxy that does not emit light and is invisible.

1.3 Summary

Even though there is evidence that dark matter exists, its nature has not been established. The scientific community at this point proposes extensions to the current standard model of particle physics. This extension usually involves a particle or class of particles that have certain properties from which interaction cross-sections can be theorized. Both direct and indirect searches for the dark matter particle suffer from the fact that the rate of interactions are functions of many parameters, for example, both the density of dark matter and the velocity distribution of dark matter in our galaxy; these will affect the flux of dark matter particles that can potentially interact with a detector. Unfortunately, both of these are model-dependent but some information can be obtained from observing spiral galaxies as was presented with the Vera Rubin's galactic stellar rotation curves. Many distributions of dark matter in spiral galaxies can explain the observations. With careful analysis of the dynamics of our galaxy and its neighbors, a better understanding of how dark matter is distributed in our galaxy can be made.

An proposal of a candidate class of particles for dark matter is the Weakly Interacting Massive

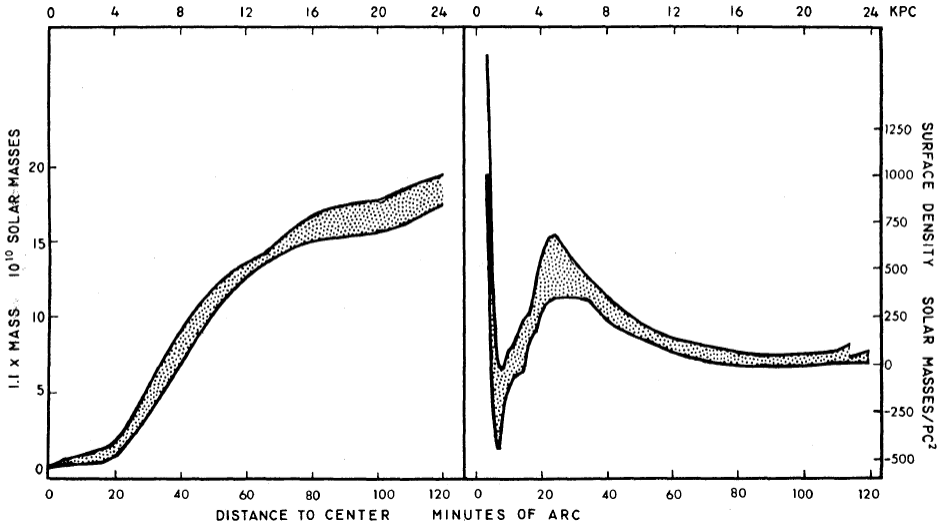

Figure 1.7: On the left, radial mass distribution of Andromeda determined by the angular velocity distribution of figure 1.2. On the right, surface mass density of Andromeda. The thickness represent the uncertainty from the measurements [3].

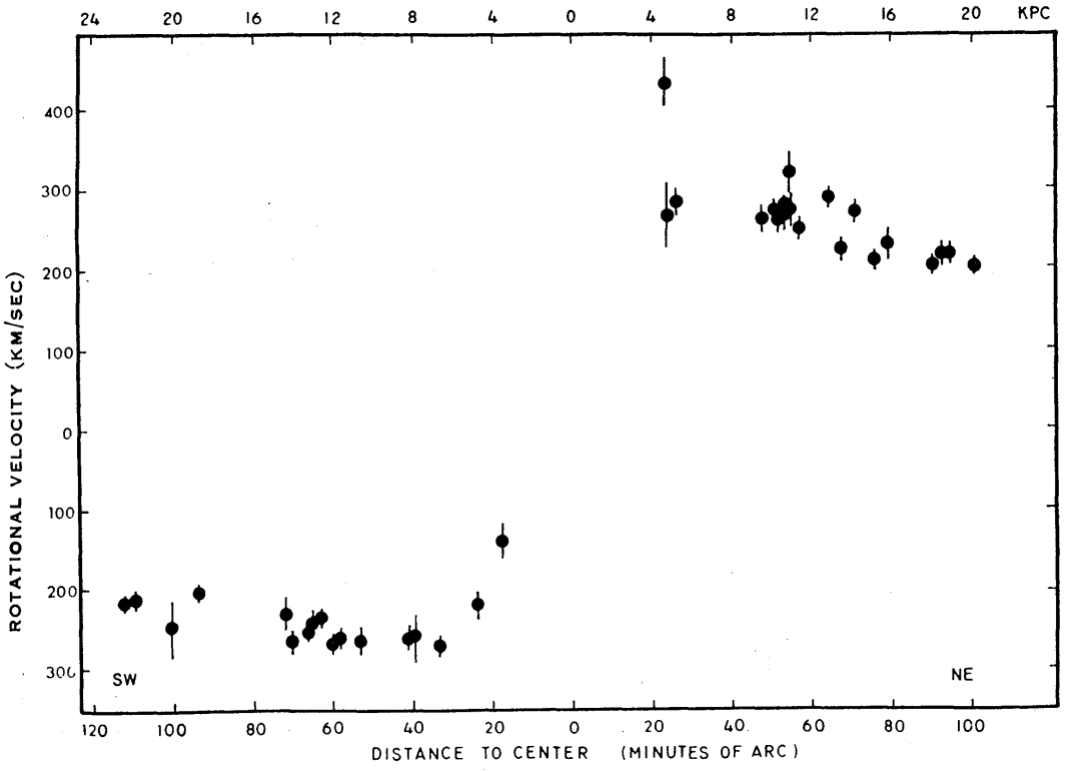

Figure 1.8: Vera Rubin's data for the angular velocities of Andromeda [3].

Particle (WIMP). Many proposed particles can fall into the WIMP class and there is a consensus that the mass of the dark matter particle should fall into below GeV/c^2 to TeV/c^2 range. There are two methods of detecting dark matter, direct and indirect. The direct detection experiments will detect interactions of dark matter with standard model particles and indirect experiments will try to detect decay products or self-annihilation products. The remainder of this thesis will focus on a direct detection experiment called PICO, the joint collaboration of two experiments, one called PICASSO, Project In Canada to Search for Super Symmetric Objects, and one called COUPP, Chicagoland Observatory for Underground Particle Physics.

Chapter 2

The PICO experiment

PICO is a direct dark matter search experiment that uses bubble chambers to detect the dark matter particle-induced nuclear recoils. In the past, bubble chambers were used to study the interactions of charged particles with the use of bubble tracks formed in the superheated liquid. As particles interact and deposit energy in the superheated liquid of the bubble chamber they leave behind a track of bubbles. The bubble chambers being immersed in a magnetic field would curve the trajectory of charged particles that allowed the study of those particles and their interactions. Superheated liquids were also used by a dark matter search experiment called PICASSO (Project In CAnada to Search for Super-symmetric Objects) beginning in 1994. PICASSO used superheated liquid droplets suspended in a gel matrix that kept the liquid or vapor contained. The very large number of droplets, of the order of millions, each acted as its own individual bubble chamber which was an innovative method at the time. An interaction of an incoming particle with a nucleus of the superheated liquid may cause a phase transition that would lead to the formation of a bubble that may

grow and vaporize the entire droplet and would emit an acoustic signal which would be captured by piezo-electric transducers. After a certain period, the detector would be re-compressed to liquify the vapor bubbles. Around 2006, another experiment called COUPP (Chicagoland Underground Observatory of Particle Physics) also used superheated liquids but instead used the full volume of the detector filled with a superheated liquid instead of droplets. After each bubble had formed, the detector would also be re-compressed so as to not have an accumulation of a vapor phase or to have an uncontrolled phase transition. Bubble growth images and acoustic signals were recorded by cameras and piezo-electric transducers, respectively. In 2013, PICASSO and COUPP combined to form the PICO collaboration. This chapter is devoted to the PICO experiment by describing the detector and the sources of backgrounds to the experiment. This will be done by examining the possible backgrounds, and the techniques to reduce and shield from these backgrounds. Finally, the latest results of PICO will be presented.

2.1 The PICO-60 Detector

A bubble chamber is often referred to as a threshold detector because all local energy depositions above the threshold amount will nucleate a bubble, but also because the initial energy of the dark matter particle, or any particle, is lost and the detector only provides a lower limit to the particle's energy. The thermodynamic conditions of the superheated liquid, i.e. the working pressure and temperature of the liquid, give a unique pair of values according to the most recent model: the radius of a bubble at equilibrium and the nucleation threshold energy. The radius of the bubble at equilibrium is used to determine the spherical region in which the energy has to be deposited to

nucleate the bubble. A detailed explanation of how to calculate the radius of the region in which the energy has to be deposited and the nucleation threshold energy is described in appendix A. Once the energy is deposited, all bubbles that nucleate are called an event and they will grow and cause an acoustic wave that will be recorded. PICO has the ability to use different types of superheated liquids, also called active fluids or target fluids as in figure 2.1. PICO utilizes C_3F_8 for operational and physics reasons. For operational reasons, it is desirable to use an active fluid whose boiling point is low at, or near, atmospheric pressure to reduce the engineering complexities. Additionally, C_3F_8 has much lower toxicity than previously used active fluids such as CF_3I, therefore any spills or other accidents do not require special alarms and procedures. As for the physics reasons, different active fluids probe different phase spaces of the dark matter model. For example, CF_3I, used in the past by COUPP, is a better probe for the spin independent models whilst C_4F_{10} and C_3F_8 are better probes for the spin dependent models. In the current dark matter model, the Weakly Interacting Massive Particle (WIMP) is the most widely accepted particle to be dark matter. The interaction cross section of the WIMP with standard matter is given by the following relation equation [8]:

$$\sigma = 4G_F^2 \left(\frac{M_\chi M_A}{M_\chi + M_A} \right)^2 C_A F(q^2) \tag{2.1}$$

where G is a coupling constant, M_A is the mass of the target with A as the atomic mass, χ is the symbol used to represent a dark matter candidate, $F(q^2)$ is a nuclear form factor that depends on the 4-momenta transfer q and C_A is an enhancement factor that depends on both the atomic number of the target and the phase space. There are two phase space possibilities to probe, either

spin dependent or spin independent. The spin independent factor can be written as,

$$C_A^{SI} = \frac{1}{4}(Zf_p + (A-Z)f_n)^2 \ , \tag{2.2}$$

where Z is the number of protons and $f_{p,n}$ are form factors for the proton and neutron respectively. The factor C_A can be maximized by large A targets. The spin independent factor can be written as,

$$C_A^{SD} = \frac{8}{\pi}(a_p < S_p > + a_n < S_n >)^2 (J+1)J \ , \tag{2.3}$$

where $(J+1)J$ is a multiplicity term of the total spin of the particle, $a_{p,n}$ are form factors that are different for either proton or neutrons respectively and $< S_{p,n} >$ are the average spins of the protons or neutrons of the target. Decoupled particle spins will maximize C_A^{SD}. Therefore, the active fluid used by COUPP, CF_3I, would maximize the spin independent factor due to the Iodine. PICASSO used and PICO uses pure fluorocarbons to maximize the spin dependent factor due to fluorine having an uncoupled proton. The rest of the following description follows the depiction of the PICO-60 detector in figure 2.1.

Once an event occurs, cameras record the bubble growth for the triggering of data acquisition and data analysis. At the top of the jar containing the C_3F_8, a ring of piezoelectric transducers convert the acoustic wave into an electronic signal that is recorded by the data acquisition system. A disassembled piezo and the piezo ring are shown below, in figure 2.2. Between the superheated liquid and the top of the jar is a buffer liquid that is used to separate the active fluid from the mechanical moving parts on top of the jar. A dytran, a type of pressure sensor, is present in the buffer fluid and measures the differential pressure as a function of time. The data from the dytran

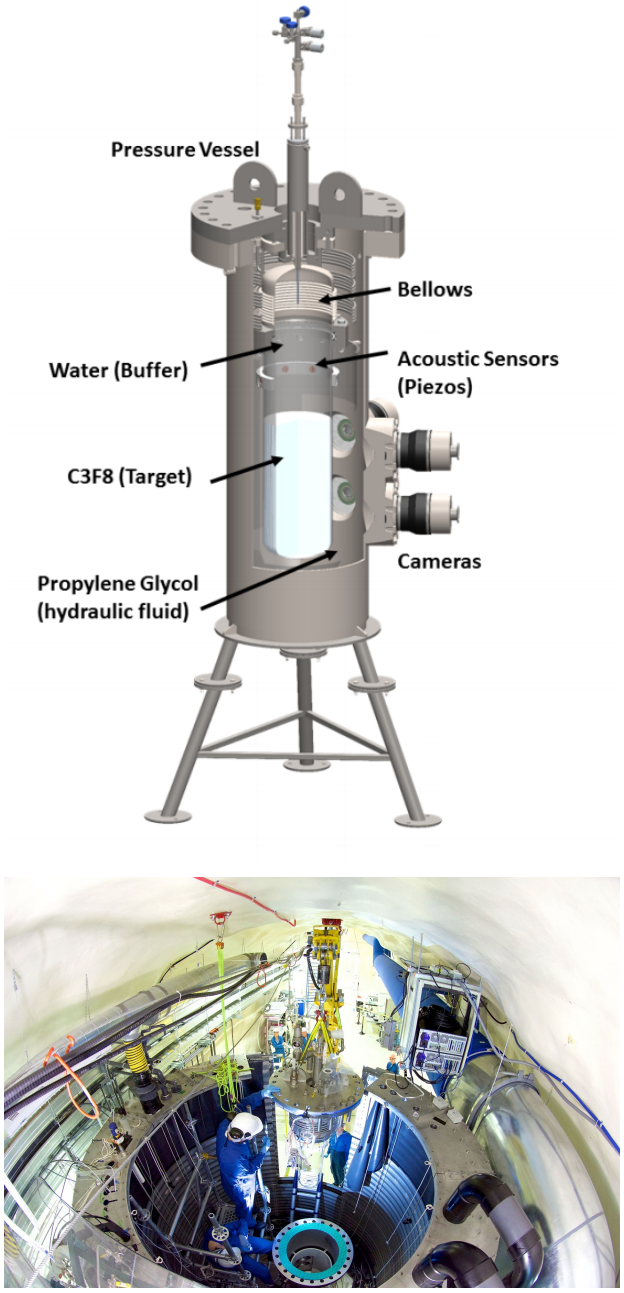

Figure 2.1: The top plot shows a schematic of the PICO-60 detector. The bottom plot shows a top view of PICO-60. The fused silica vessel is outside of the pressure vessel and the the pressure vessel is beside the workers knees.

is used to accurately count bubbles in a multi-bubble event. Both the buffer and the active fluid are contained in a fused silica vessel attached to a bellows system. The bellows is a one-sided open metallic cylinder with accordion walls that forms the top of the fused silica vessel. The cylinder

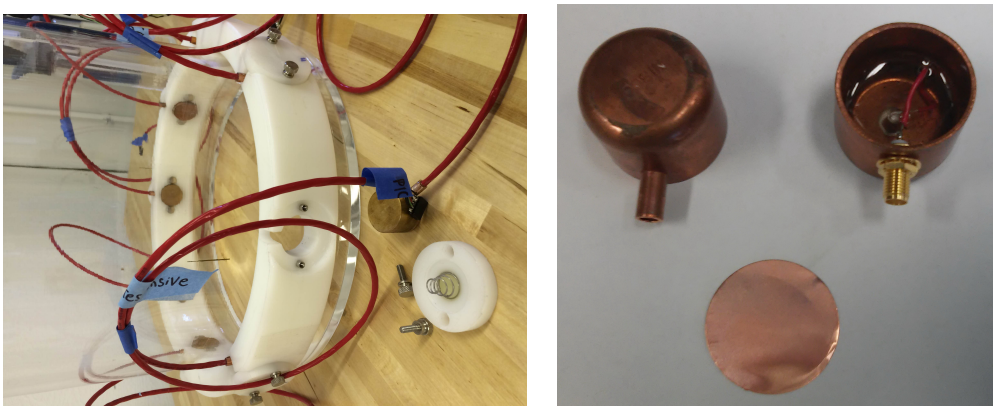

Figure 2.2: The left picture shows a ring of piezoelectric transducers. The right picture shows a disassembled piezoelectric transducer.

is open to the inside of the jar. The bellows transfer the pressure from the outside to the inside of the jar or vice-versa. The inside of the bellows is in contact with the buffer liquid that controls the pressure of the active fluid. Propylene glycol is the fluid of choice for the hydraulic fluid to push on the bellows from the outside. The fused silica vessel and the bellows are both inside the pressure vessel and immersed in the hydraulic fluid that also serves as a heat exchanger to control the temperature of the active fluid. The entire apparatus of figure 2.1 is submerged in ultra pure water to shield the detector from outside neutrons. The water may also be used to create Cherenkov light due to the passage of muons that can be detected by adding photomultiplier tubes (PMT) at the top of the water tank as depicted in figure 2.3. This muon detector was part of my work for the collaboration. The purpose of the muon detector is to input to the data acquisition system the time at which a muon was detected. This allows events within a time window surrounding the time of detection of the muon to be removed from analysis.

Once the acoustics of an event are recorded, the piezo signals are used in the analysis to form the Acoustic Parameter (AP) histograms as depicted in figure 2.4. The AP value of an event involves a spectral analysis of the acoustic signal. From calibration events, certain frequency bins are used in

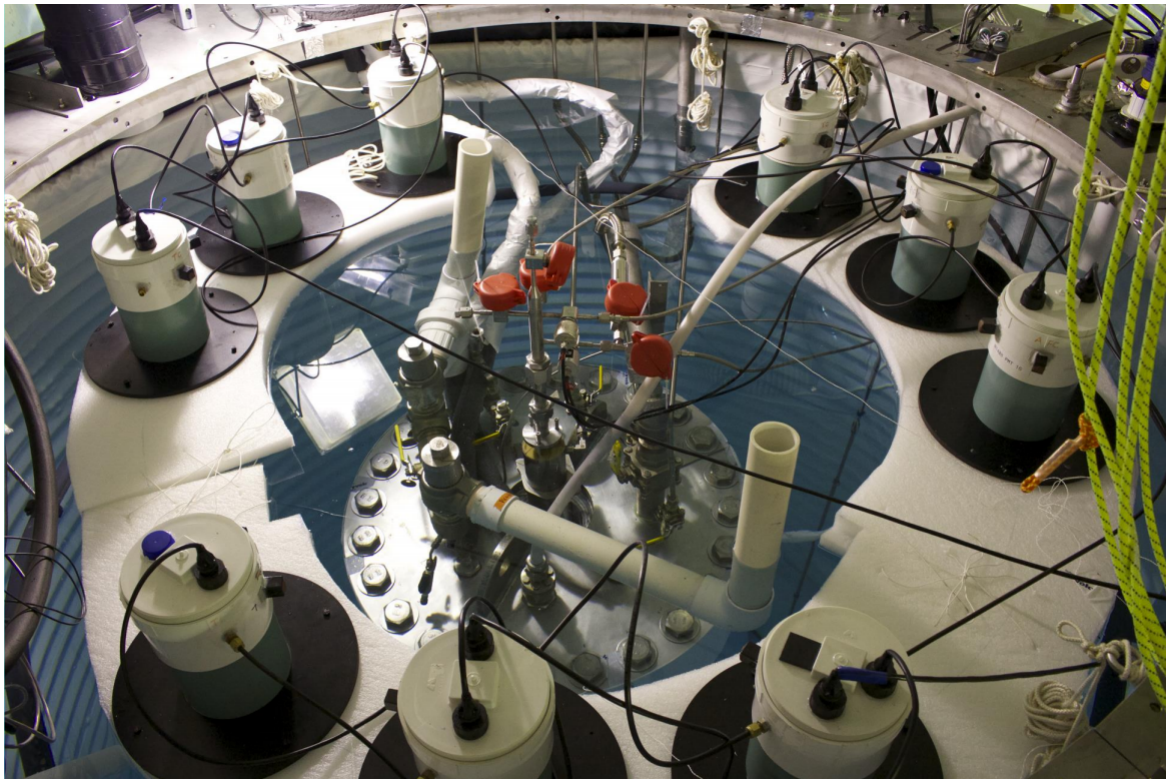

Figure 2.3: Muon veto system of PICO-60

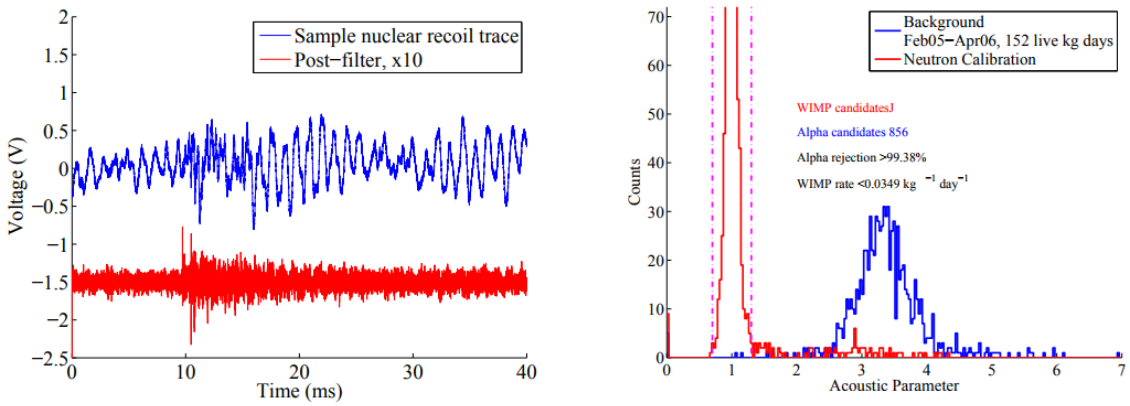

Figure 2.4: The left image shows two plots: the top plot is a raw acoustic signal and on the bottom is the processed acoustic signal. The right image contains the Acoustic Parameter histograms produced from the processed acoustic signals.

a weighted sum and corrected for normalization. Calibrations are controlled emission experiments to assess how the detector responds. There are several types of calibrations devices which can be deployed, for example, gamma calibrations, neutron calibrations, alpha calibrations, etc. Alpha

calibrations are typically done on smaller bubble chambers as they contaminate the detector. Neutron and gamma calibrations can safely be done without affecting the detector and are the most common. The spectral analysis of alpha events, neutron events and noise are depicted in figure 2.5. The frequency bins that are selected to calculate the AP are frequencies that maximize the

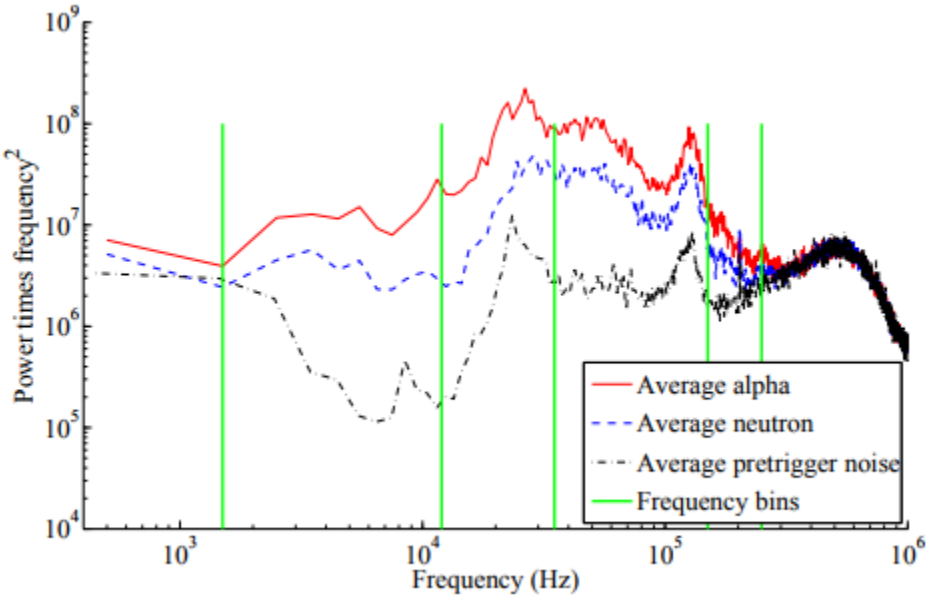

Figure 2.5: Power Spectral Density with noise minimized.

separation of the AP histogram of figure 2.4 during calibrations. Several corrections are performed to have the AP of neutron calibration events normalized to one.

Events with multiple bubbles are most likely triggered by neutrons due to their mean free path being less than the diameter or height of the jar of the detector. The probabilities for events with more than 2 bubbles can be evaluated by Monte-Carlo simulations. Therefore, the occurrence of these types of events can tabulated and compared with simulations to assess the validity of the model.

2.2 Backgrounds

One of the most important design aspects of an experiment is to be able to predict what should be observed. The standard model of particle physics contains all the information to allow the calculation of interaction cross-sections of all known particles with nuclei of the active fluid. This would be unfeasible to be done by hand, but fortunately various software packages can be used to model the backgrounds. The most widely used software is GEometry And Tracking [13]. The software uses the most up to date cross sections of interactions to track the passage of particles within a given geometry. The geometry can be as complex as desired and the physics to be included can be also be tailored to the needs of the user. Information to be injected into the background model come from various types of material assays. The background model's purpose, in the end, is to estimate a rate of events in the detector from backgrounds. Understanding and quantifying all backgrounds is crucial to be able to ascertain that an event rate above the expected rate of is in fact a discovery and not an unquantified background. This section will cover the known backgrounds of PICO-60.

Many different types of particles can interact and deposit energy within the superheated liquid and cause a bubble or multiple bubbles. All bubbles caused by a particle form an event. All particles that can cause an event and are not dark matter are backgrounds. The main backgrounds are alphas and neutrons. Other backgrounds, which are orders of magnitude less important, include photons, electrons and neutrinos. It is to be noted that the importance of certain particles as backgrounds is a function of the threshold of the detector. In the current state of PICO-60, for example, the probability of a photon to nucleate a bubble is of the order of 10^{-10} for a 6 keV threshold. Dropping the

threshold would increase the nucleation probability to a level that is no longer negligible. Similar arguments can be made for other particles. The primary task of the experiment is to identify all possible sources of background and to reduce or shield those backgrounds. PICO is located at SNOLAB, an underground laboratory situated at a depth of 2 kilometers inside Vale's Creighton mine in Sudbury, Ontario.[1]. The layout of SNOLAB is depicted in figure 2.6 Being deep under-

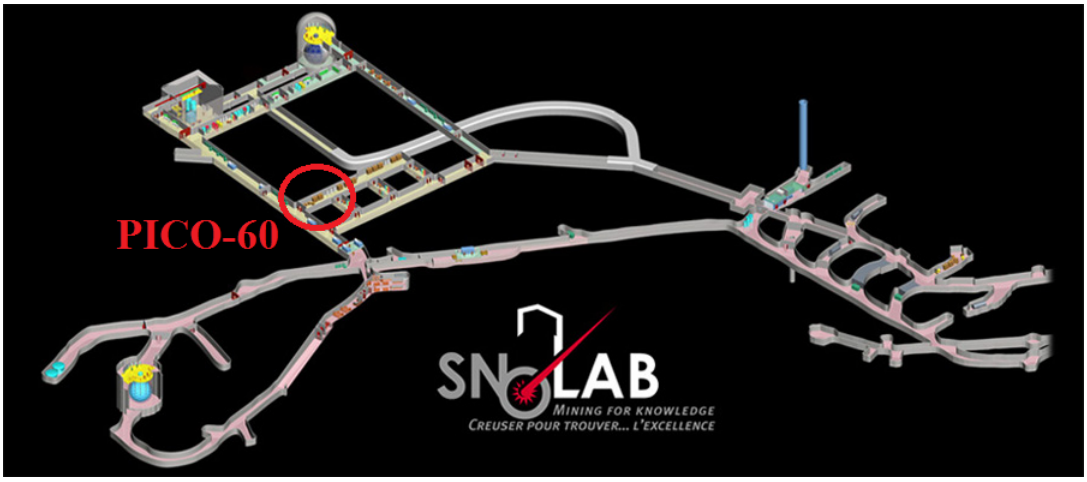

Figure 2.6: Schematic of SNOLAB.

ground shields the detector from showers of high energy particles induced by cosmic rays. But nonetheless some particles, for example muons and neutrinos, still make it to the laboratory and have the possibility of interacting with materials and cause backgrounds. Even being underground still has its challenges, the surrounding mine rock can cause backgrounds; and all the materials of the detector and even the air, which contains radon, may directly or indirectly cause backgrounds. This is why it is crucial to understand each background, their source and how to shield the detector from them.

[1]For more information: http://www.snolab.ca/

2.2.1 The Alpha Particle Background

Alpha particles are the result of decays from radioactive nuclei. These nuclei are present in all materials surrounding the detector. The uranium and thorium decay chains are the two main sources of alpha particles. Other sources of alphas may be removed via purification processes, but uranium and thorium are particularly hard to purify due to their low concentration and presence in nearly all materials. One of the radioactive members of the uranium chain is an isotope of Radon, ^{222}Rn, which has a relatively long half-life of 3.8235 days and may be present on its own in the air and in materials. The concentration of contaminants varies from material to material but this is assessed with the aid of assays. To determine the concentration of radioactive contaminants, germanium detectors are used. Germanium detectors fall under the category of semiconductor detectors. When the germanium is operated as a diode, the ionization of the germanium nuclei by the photons can be used to infer the energy of the photon. Thus, a spectrum of energies from radioactive decays may be produced which may be used to determine the concentration of a particular contaminant. The uranium and thorium decay chains are presented in tables 2.1 and 2.2, where the energy of the different gammas, alphas and betas are tabulated. Reducing the alpha particle background is done by having strict standards for purity of materials to minimize radioactive contamination. A characteristic of the alpha particle is its short travel distance, of the order of micrometers, therefore only alpha particles produced near the edge of the fused silica in contact with the superheated liquid will have a chance to cause an event. Events close to the walls can be removed from the analysis. The active fluid's contaminant concentration is non-zero and may cause events. These events require some analysis and are removed with the Acoustic Parameter. It was first observed in Picasso that events from alpha particles were louder than nuclear recoil events. This led to the

development of the Acoustic Parameter as discussed earlier. High AP scores are typical of alpha events whereas neutron calibration events would be normalized to a score of one. The AP helps discern and cut possible alpha events from radioactive decays that propagated far from the wall or from radioactive contamination present in the C_3F_8.

2.2.2 The Neutron Background

Neutrons can be produced by spallation from high energy muons, through (α, n) or (γ, n) reactions with the materials and the mine rock surrounding the detector. Neutrons are notorious because of how they interact in the superheated liquid that is indistinguishable from the WIMP interaction. This is why it is crucial to have low radioactive contamination for the materials surrounding the detector and shielding the detector from neutrons from the mine rock. An effective method for shielding from neutrons outside the detector is submerging the detector in ultra-pure water to moderate the neutrons. The energy of the moderated neutrons are of too low to cause events within the active fluid. Spallation neutrons caused by muons are cut by detecting the muon. This is achieved by detecting the Cherenkov radiation caused by muons traversing the ultra-pure water of the water tank. A ring of photomultiplier tubes is setup on top of the water shielding tank to detect that radiation. Once a muon is detected, all events around the time of detection are removed from analysis. For neutrons of high energy that are generated inside the detector, one characteristic that can be used to distinguish them from others types of events is the mean free path of interaction. The mean free path is of the order of centimeters that is small relative to the size of the detector. Therefore, those neutrons can interact multiple times along their path through the detector causing an event with multiple bubbles. This leads to a new cut where events with multiple bubbles are

removed from the analysis. The multiplicity of an event, i.e. the number of bubbles present, can be tracked with the dytran and the cameras. Tracking multiple bubbles is the most effective method of quantifying the neutron background.

2.2.3 Other Backgrounds

Photons and electrons have similarities that make them easier to be grouped together. These particles are products of radioactive decays of uranium and thorium that are presented in tables 2.1 and 2.2. These particles will deposit their energy mainly through electromagnetic interactions. In the operating conditions of the detector, the electron will never transfer sufficient energy via elastic collision with nuclei to surpass the threshold. The predominant mode of energy loss for electrons is by ionization. It is currently being investigated if electrons at the current thresholds used by PICO of [1.2-3.3] keV can cause events and what should be the expected rate [5]. For the photon, the elastic and inelastic scattering cross sections are both functions of its energy. Together with the continuous electromagnetic energy deposition and the most recent threshold of the detector the probability of a photon nucleating a bubble is of the order of 10^{-10} for a threshold of 6 keV that is negligible [5].

Neutrinos are the next source of noteworthy backgrounds. The neutrino has a very small interaction cross section but can still cause events for detector thresholds below 5 keV from coherent scattering with a nucleus. Only the ^{8}B solar neutrinos have the energy and flux to be of concern [5]. Since neutrinos cannot be shielded against, when the detector reaches sufficiently low thresholds it will be capable of detecting neutrinos. It is important to realize that, at least for PICO, whenever an

event occurs a process of recompression and stabilization that lasts approximately 100 seconds is initiated. Every tenth event the recompression time is increased to 600 seconds. During this time the detector is termed dead or inactive.

Particulates are a completely separate entity in terms of backgrounds; they cause events from a different type of nucleation. When a phase transition occurs within the bulk of the liquid, this is termed homogeneous nucleation. Bubbles that are nucleated within the bulk are also part of homogeneous nucleation. Bubbles that are nucleated on surfaces of pores or nucleated from impurities are referred to as inhomogeneous nucleation. Particulates are a form of impurity, they can be macroscopic or microscopic and have rough or porous surfaces that can cause inhomogeneous nucleation. The events from particulates do not have any specific AP characteristics and are therefore problematic. Having a strict level of purity for the active fluid mitigates the problem of particulates initially, but having the detector run for long periods of time still has particulates accumulate in the active fluid from the bellows. As the bellows recompress the active fluid, they shed small amounts of material that make their way into the active fluid and cause inhomogeneous nucleation. This problem has lead PICO to research new designs for the detector. The simplest solution was rotate the jar upside down and redesign the compression system. This was the birth of PICO-40L and, possibly, all future generations of detectors.

Element	Decay Type	Energy(keV)(%)
$^{238}_{92}$U	α	4151(20.9), 4198 (79.0)
$^{234}_{90}$Th	α	86.87(2.9), 106.28(7.6), 106.7(19.2), 199.08(70.3)
$^{234m}_{91}$Pa	β^-	1224.39(1.007), 2268.92(98.2)
$^{234}_{92}$U	α	4722.40(28.42), 4774.6(71.38)
$^{230}_{90}$Th	α	4620.5(23.4), 4687.6(76.3)
$^{226}_{88}$Ra	α	4601(5.55), 4784.34(94.45)
$^{222}_{86}$Rn	α	5489.52(99.92)
$^{218}_{84}$Po	α	6778.3(99.9981)
$^{218}_{85}$At	β^-	158.53(5.17), 335.17(82.5), 573.8(12.3)
$^{214}_{83}$Bi	β^-	789.54(1.33), 824.3(2.81), 1067.87(5.72), 1153.45(4.26) 1254.7(2.20), 1261.19(1.37), 1277.37(1.14), 1381.71(1.59) 1424.57(8.8), 1507.5(17.02), 1542.39(17.08), 1728.63(2.95) 1894.32(7.43), 2662.68(1.7), 3272(18.2)
$^{214}_{82}$Pb	α	8784.37(100)
$^{214}_{83}$Bi	α	5273(5.8), 5452(53.9), 5516(39.2)
$^{214}_{84}$Po	α	7686.82(99.9895)
$^{210}_{81}$Ti	β^-	1384(2), 1609(7), 1864(24), 2029(10) 2419(10), 4210(30, 4391.3(20)
$^{210}_{82}$Pb	β^-	16.96(84), 63.5(16)
$^{210}_{83}$Bi	β^-	1162.1(100)
$^{210}_{84}$Po	α	5304.38(100)
$^{206}_{82}$Pb	stable	0
$^{206}_{80}$Hg	β^-	657.58(3.5), 1002.1(42), 1307(54)
$^{210}_{83}$Bi	α	4656(60), 4694(40)
$^{206}_{81}$Ti	β^-	1522.5(99.9)
$^{206}_{82}$Pb	stable	0

Table 2.1: Uranium Decay chain, metastable states are noted with a lower case m in the left superscripts. Standard convention was used, the left superscript is the atomic weight, the left subscript is the atomic number [9].

Element	Decay Type	Energy(keV)(%)
$^{232}_{90}$Th	β^-	3811.1(0.069), 3947.2(21.7), 4012.3 (78.2)
$^{228}_{88}$Ra	β^-	12.83(30), 25.71(20), 39.23(40), 39.62(10)
$^{228}_{89}$Ac	β^-	1730.30(11.66), 1158.03(29.9), 1104.47(3.16), 1004.05(5.92) 958.63(3.08), 595.53(8), 488.72(1.15), 481.05(4.16) 444.19(1.12), 438.61(2.45), 402.72(1.76)
$^{228}_{90}$Th	β^-	5340.36(27.2), 5423.15(72.2)
$^{224}_{88}$Ra	β^-	5448.6(5.06), 5685.37(94.92)
$^{220}_{86}$Rn	β^-	6288.08(99.886)
$^{216}_{84}$Po	β^-	6778.3(99.9981)
$^{212}_{82}$Pb	β^-	158.53(5.17), 335.17(82.5), 573.8(12.3)
$^{212}_{83}$Bi	β^-	633.26(1.87), 741.3(1.43), 1526.67(4.36), 2254(55.46)
$^{212}_{84}$Po	α	8784.37(100)
$^{208}_{82}$Pb	stable	0
$^{212}_{83}$Bi	α	5607(1.19), 5768(1.78), 6050.78(69.91), 6089.88(27.12)
$^{208}_{81}$Ti	β^-	1040.04(3.09), 1292.56(24.5), 1525.89(21.8), 1803.26(48.7)
$^{208}_{81}$Pb	stable	0

Table 2.2: Thorium decay chain. Standard convention was used, the left superscript is the atomic weight, the left subscript is the atomic number [9].

2.3 Predicting The Event Rate

The process of predicting an event rate starts off with the following formula,

$$dR = \frac{N_0}{A}\sigma v dn \ , \tag{2.4}$$

where N_0 is the Avogadro number, A is the atomic mass in AMU of the target, σ is the interaction cross section of the particle with the target, v is the velocity of the interacting particle, dn is number density of the interacting particle. In an experiment, it is the sum of all contributions to the rate that is observed such that

$$dR_{obs} = \sum_i \frac{N_0}{A}\sigma_i v_i dn_i \ , \tag{2.5}$$

$$dR_{obs} = dR_{DM} + dR_{BG} \ . \tag{2.6}$$

Quantifying the flux of background particles can be done and cross section information can be found in most particle physics textbooks, for example, Griffiths [11] or the Particle Data Group reference book [12]. Simulation software such as GEANT4 can be used to predict the event rate from backgrounds [13]. What is left is the dark matter contribution, but most of the parameters are unknown. If the dark matter velocity is assumed to be a Maxwell-Boltzmann distribution, and the interaction cross section can be approximated as constant at least for low momenta transfer then

the event rate spectrum can be simplified to the following formula [14]

$$\frac{dR}{dE_R} = \frac{R_0}{E_0 r} e^{-E_R/E_0 r}, \tag{2.7}$$

$$r = 4\frac{M_D M_T}{(M_D + M_T)^2} \ , \tag{2.8}$$

$$R_0 = \frac{2}{\pi^{1/2}} \frac{N_0}{A} \frac{\rho_D}{M_D} \sigma_0 v_0 \ , \tag{2.9}$$

where E_0 is the most probable kinetic energy of the dark matter particle of mass M_D, E_R is the recoil energy, r is a kinematic factor for a target nucleus of mass M_T. Observational data similar to the stellar rotation curves of Vera Rubin's [3] for the Andromeda galaxy give an estimate for the dark matter density of our galaxy. Certain references of Lewin [14] propose different constraints for the dark matter escape velocities, the Earth's velocity and the sun's velocity that are used to to get to equation 2.7. This event rate formula is oversimplified and has multiple corrections of the form

$$\left.\frac{dR}{dE_R}\right|_{obs} = R_0 S(E) F^2(E) I \ , \tag{2.10}$$

where S would correct for the detector efficiency, having multiple targets, instrumental resolution, etc. F is a form factor correction for higher momenta transfers and I is an interaction correction for spin-dependent or spin-independent factors [14].

2.4 Latest Results

The most recent results of PICO were taken with the PICO-60 detector filled with 52.2 ± 0.5 kg of C_3F_8. The efficiency corrected exposure was 1167 kg· day. Strict cleaning procedures for

the active fluid and buffer fluid followed the military standard MIL-STD-1246 and met the level 100 [15]. GEANT4 simulations predicted a neutron background of 0.25 ± 0.09 single bubble events and 0.96 ± 0.34 multiple bubble events for the given exposure. The detector was exposed to a 1 mCi ^{133}Ba source before and after the physics runs and compared to the GEANT4 simulation to give a nucleation efficiency for electron recoil events above 3.3 keV of $(1.80 \pm 0.38) \times 10^{-10}$. Combining this with the GEANT4 simulation for the external gamma flux yielded a prediction of 0.026 ± 0.007 events due to electron recoils for the given exposure. Finally the background from ^{8}B neutrinos was calculated for the given exposure to be 0.055 ± 0.007 events. The acoustic analysis procedure is described in reference [16], with the cuts describe in that reference, the WIMP search event candidates gave the AP distribution shown in figure 2.7. Exclusion plots are used to show the

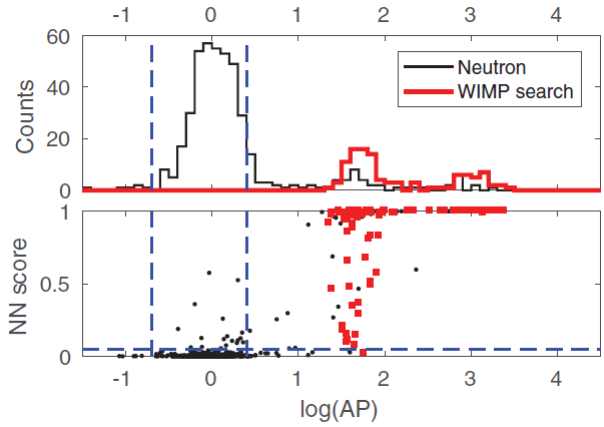

Figure 2.7: Latest AP plot of the PICO-60 [5].

phase space probed by the experiment. For example, PICO presented both figures of 2.2 for our latest results. An exclusion plot is a plot of the dark matter interaction cross section with respect to the dark matter mass inferred from the corrected event rate of equation 2.8. As discussed earlier, PICO searches for the WIMP in both the spin-independent and spin-dependent models, hence the two figures of 2.8. Both these models have cross sections that are functions of the atomic number

or the amplification factor as defined in equations 2.2 and 2.3. For a given detector threshold, the detector can probe all phase space above its respective line. They are called exclusion plots because they present the probed phase space that did not yield a successful dark matter event. It is customary to present the exclusion plots of other experiments to compare and confirm that the phase space is indeed excluded. It is also useful to present the phase space predicted by other theories and usually these are shaded areas.

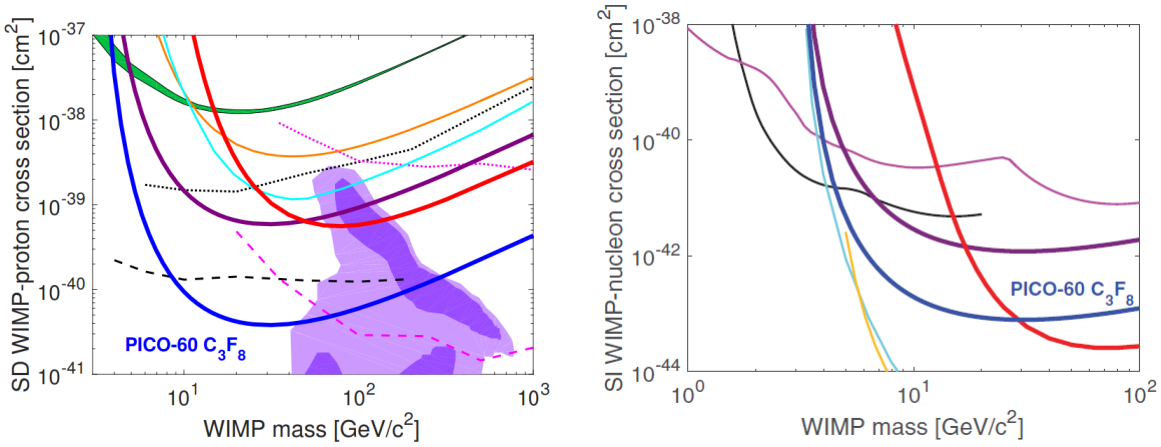

Figure 2.8: The left plot shows spin-dependent WIMP-proton interaction cross section as a function of mass. The right plot shows the spin-independent WIMP-proton interaction cross section as a function of mass [5].

Chapter 3

Bubble Growth Dynamics

In the previous chapter, it was shown that the acoustic signal of an event is an important part of the analysis and contains information that allows the discrimination between alpha particle events and nuclear recoil events. The acoustic wave detected by the piezos is a result of a bubble or bubbles growing in the superheated liquid. The acoustic intensity emitted by the growing bubble is proportional to the second derivative of the volume of the bubble with respect to time, $\ddot{V}$. On that account, we put forward the hypothesis that the rate of growth of the bubble itself may also contain information to discriminate alpha particle events from nuclear recoil events. The work of H. S. Lee and H. Merte [17] showed that a bubble initially at equilibrium in superheated liquid can grow given that the equilibrium conditions are perturbed. The perturbation can be either a change in the bubble's size, vapor temperature, vapor pressure, etc. These authors mainly focused on the vapor temperature perturbation and investigated the effects of three temperature disturbances, 10^{-1} °C, 10^{-5} °C and 10^{-12} °C. Their results showed that the magnitude of the perturbation influenced

the rate growth of the bubbles significantly. Firstly, the interface velocities early in the bubble growth had 10 orders of magnitude difference between bubble growths triggered by temperature disturbances of 10^{-1} °C and 10^{-12} °C. Secondly, the magnitude of the perturbation affected the time it took for the bubbles to begin growing.

According to the thermodynamic model used by PICO, if the nucleation threshold energy is deposited by a particle within the nucleation region, a bubble may be nucleated in a state of equilibrium and any excess energy deposited within the region will allow the bubble to grow [27]. In view of the work by H. S. Lee and H. Merte, one could infer that all the excess energy within the nucleation region will be used to increase the vapor temperature of the bubble. This increase in temperature is the temperature disturbance described in their article [17]. A legitimate question then arises: can these temperature disturbances be used to describe the energy deposition of alpha particles or nuclear recoils, for example, from neutrons?

3.1 Investigating Temperature Disturbances

This section will answer the following question: can the temperature disturbances describe the energy deposition of different particles? In the context of the WIMP dark matter search, nuclear recoils initiated by neutrons interactions are expected to mimic dark matter recoils. The nuclear recoil energy is expected to range from 1 keV to 100 keV [14]. Carbon or fluorine recoiling with energies in that range may nucleate bubbles with excess energies that will, according to the model being studied, produce temperature disturbances that map, one-to-one, these energies. Given that alpha particles from radioactive decays are much more energetic, in the MeV range, than the

nuclear recoils considered here, alpha particles should generate higher temperature disturbances. The formalism to investigate the question follows.

In the context previously described, alpha particles lose energy continuously. The same may be said for carbon and fluorine ions. The Bethe-Bloch formula [18] can be used to calculate an estimate of the mean stopping power due to ionization of a charged particle passing through matter. In addition, various simulation software such as GEometry ANd Tracking 4, GEANT4 [13], and TRansport of Ions in Matter, TRIM [23][24], are readily available and use up-to-date interaction cross sections to fully describe the passage of ions through matter. These software makes use of the Monte-Carlo method to simulate the passage of an ion through a target volume. There are two caveats to these software though: first, the target volume is not modeled as molecules of C_3F_8 in the liquid state but instead as an aggregate of carbon and fluorine atoms with the appropriate stoechiometric ratios and density. Second, the target is at a temperature of 0 K. The TRIM software attempts to tabulate the energy of the ion, its position, the electronic stopping power and the energy lost to the last recoil whenever the energy lost to the last recoil is equal to or greater than a parameter input by the user. All simulations were done with an input parameter of 1 eV, i.e., the software tabulates all recoils of energy greater than 1 eV. This ensures that, most likely, all interactions of interest are tabulated. TRIM also offers the functionality of tabulating what it calls cascades. These are produced when a recoil has sufficient energy to cause a nucleus of the target volume to delocalize and deposit the energy transferred from the recoil minus a bond energy for the selected target. Figure 3.1 shows an example track of a 1 MeV alpha particle, zoomed near to its end, where the Bragg peak occurs. At the Bragg peak, the stopping power is maximal. This is due to the electromagnetic interaction cross section being inversely proportional to the square of the kinetic energy of the ion. Therefore,

the energy lost by the particle increases with decreasing energy due to the number of interactions that increase at low energies [12].

To calculate the radius of the region and the nucleation threshold energy of the superheated liquid, the temperature and pressure are required. The calculation of the nucleation threshold energy can be found in Appendix A. For a liquid to be considered superheated, it must be above the saturation temperature at a given pressure. It is possible to define the term superheat which is the difference in temperature with respect to the saturation temperature,

$$Superheat = T - T_{sat}(P) \ , \tag{3.1}$$

where T is the temperature of the liquid and T_{sat} is the saturation temperature at the given pressure of the liquid. For example, water at 1 atmosphere has a saturation temperature of 100 °C [35]. Therefore, if the liquid is said to be at a superheat of 1 °C for a liquid at 1 atmosphere, that implies the liquid is at a temperature of 101 ° C. Since the value of interest for PICO is the nucleation threshold energy, two situations can arise: a high superheat or a low superheat condition detector that can both yield the same nucleation threshold. Thus, for the remainder of this Chapter the values of table 3.1 will be used for high and low superheat condition. With these values, the equilibrium bubble radii would correspond to 19 nm for a high superheat and 17 nm for a low superheat. The region in which the energy must be deposited is related to the equilibrium bubble radius:

$$R_{region} = \left(\frac{\rho_v}{\rho_l}\right)^{1/3} R_{equilibrium} \ , \tag{3.2}$$

where ρ_v and ρ_l are the vapor and liquid densities respectively. This would yield a region of radius

condition	Superheat	Pressure	Nucleation Threshold
High superheat	88.0 °C	0.10 atmospheres	1.75 keV
Low superheat	22.0 °C	5.00 atmospheres	1.75 keV

Table 3.1: The detector conditions which are used for the calculations that refer to high superheat and low superheat.

6 nm for a high superheat and a radius of 7 nm for a low superheat.

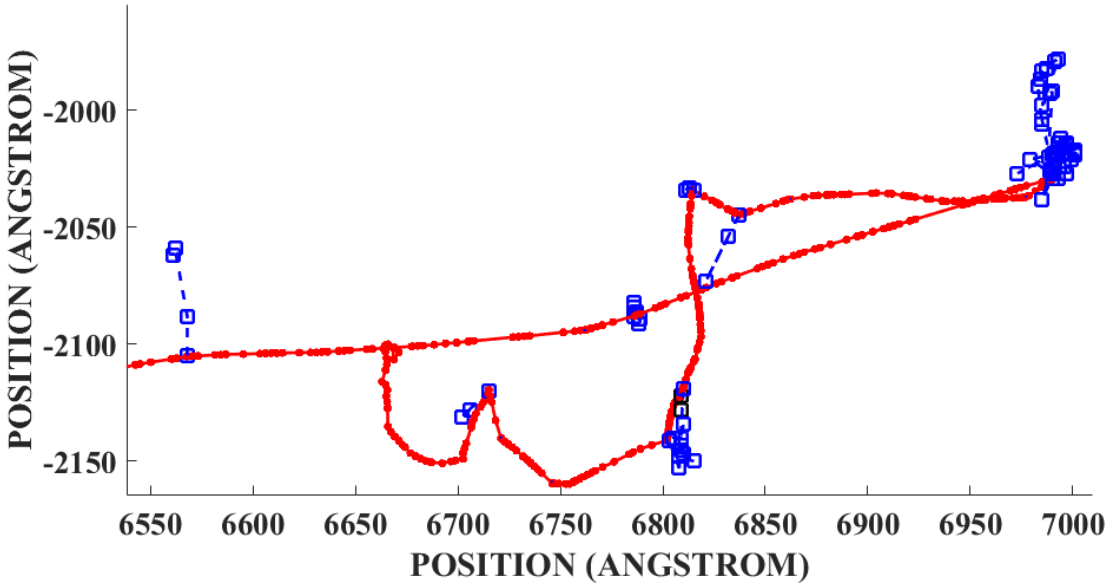

Figure 3.1: Example track of a 1 MeV alpha particle in C_3F_8 zoomed near the Bragg peak. The red doted line depicts the position of the elastic nuclear recoils and the blue squared line depicts the cascades, tracks of other fluorine or carbon ions from recoils of high enough energy to delocalize them.

It was discussed earlier that nuclear recoil energies would be expected to range from 1 keV to 100 keV. For the purpose of the TRIM simulation and other calculations, a 2, 5 and 100 keV fluorine ions were chosen. For the typical radioactive decay, a 1 MeV alpha was chosen. A fluorine ion was chosen over a carbon ion because it is the nucleus of interest for PICO's dark matter search experiment. Figure 3.2 shows an example track for a fluorine ion. A carbon ion would show a similar track. It is possible to scan the tracks to determine all possible regions that may nucleate a bubble and tabulate the excess energy within each of those regions. The procedure

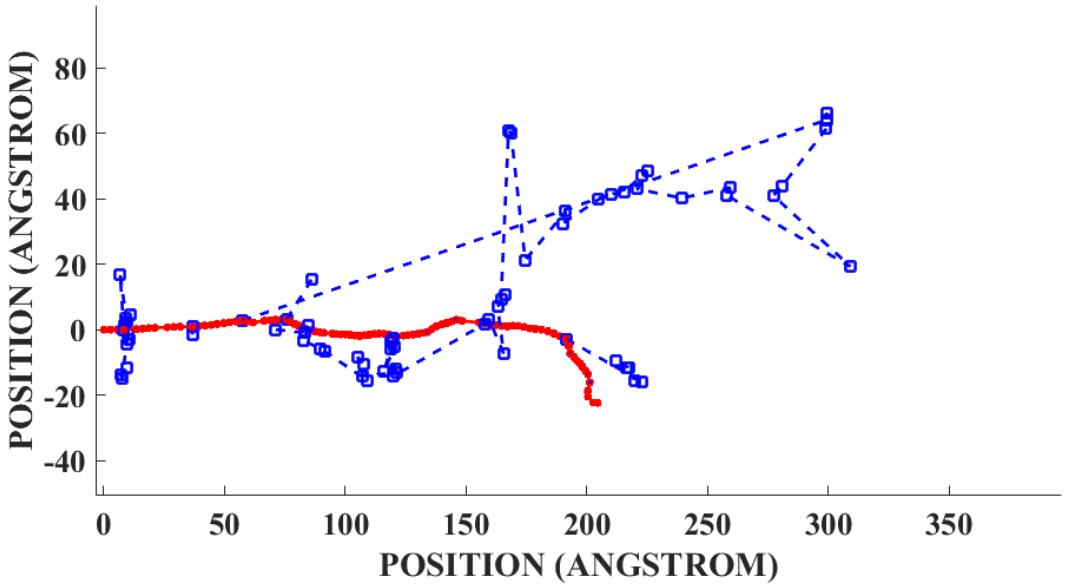

Figure 3.2: Example track due to a nuclear recoil off a carbon or fluorine. Tracks from carbon and fluorine ions are very similar, therefore only one is presented: a fluorine ion of 5 keV. The red doted line depicts the position of the elastic nuclear recoils and the blue squared line depicts the cascades, tracks of other fluorine or carbon ions from recoils of high enough energy to delocalize them.

is straightforward, each position of elastic scattering is considered as the center of a region that may nucleate a bubble. The next step is to calculate the distance to all other positions of elastic collisions and tabulate those that are within the radius of the region in which the energy must be deposited. Summing both the elastic recoils and the energy deposited by the electrons inside the region gives a first approximation to finding the possible bubbles that may be nucleated along the track. It should be noted that not all regions that satisfy the nucleation condition may contribute to nucleating bubbles. In addition, if the edge of a region lies between two interactions, the energy deposited by the electrons of the medium will be overestimated. The result of this scan is shown in figure 3.4 and 3.5. In figure 3.4, a range of nuclear recoil energies are presented to emphasize the effect of increasing the energy of the nuclear recoil, the characteristic peak present in the low energy nuclear recoils fade away in favor of populating the lower excess energies.

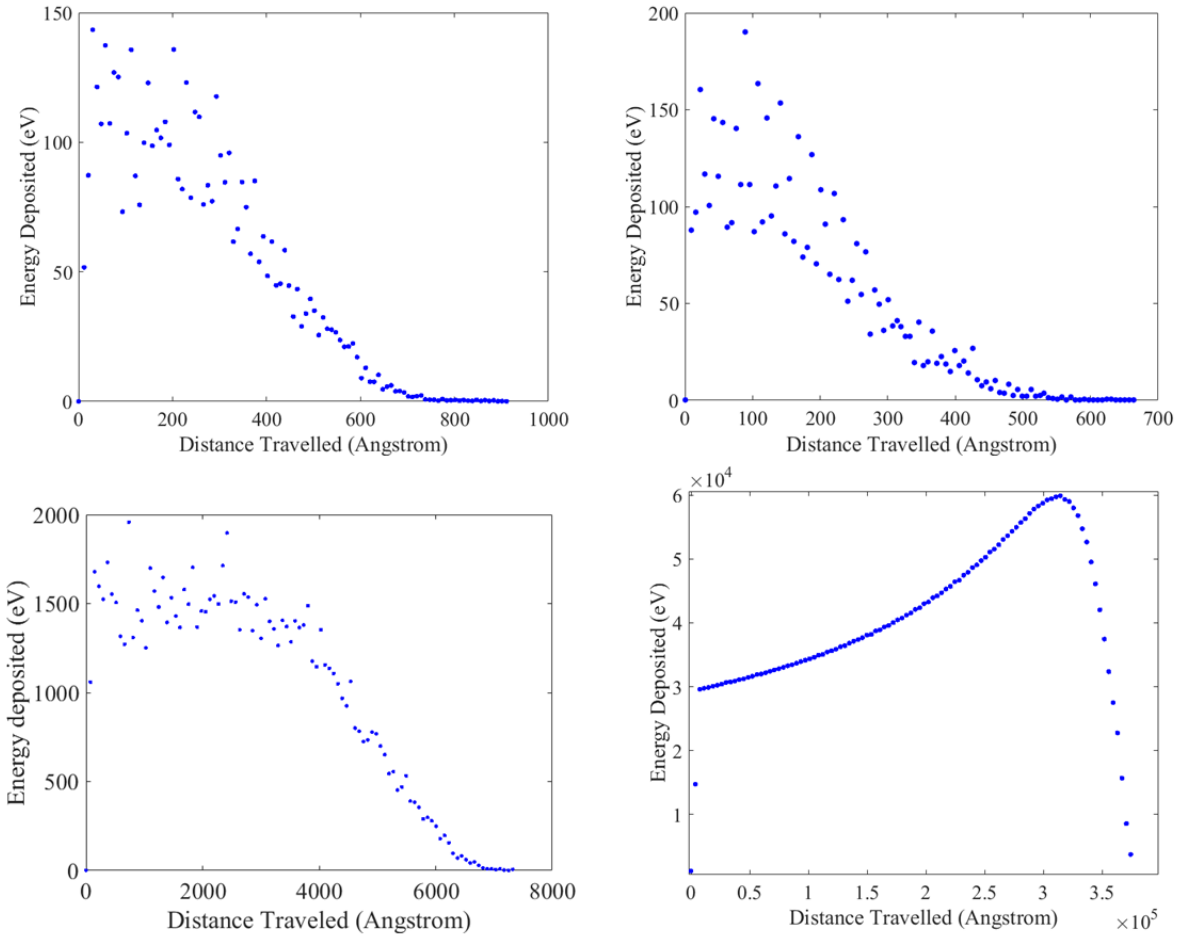

Figure 3.3: Energy deposited as a function of the distance traveled in C_3F_8 at a high superheat as described in table 3.1. The top left plot shows a 5 keV carbon ion. The top right shows a 5 keV fluorine ion. The bottom left shows a 100 keV fluorine ion. The bottom right shows a 5 MeV alpha particle. All plots were made with 500 tracks.

The last step is to calculate the vapour temperature increase to begin the numerical solution of bubble growth. This requires the average increase of energy per molecule and the ideal gas law, to relate the average increase in kinetic energy to the temperature increase. Using dimensional analysis, the following formula can be used to calculate the number of molecules

$$N = \frac{A\rho_v 4\pi r_e^3}{3M}\ , \tag{3.3}$$

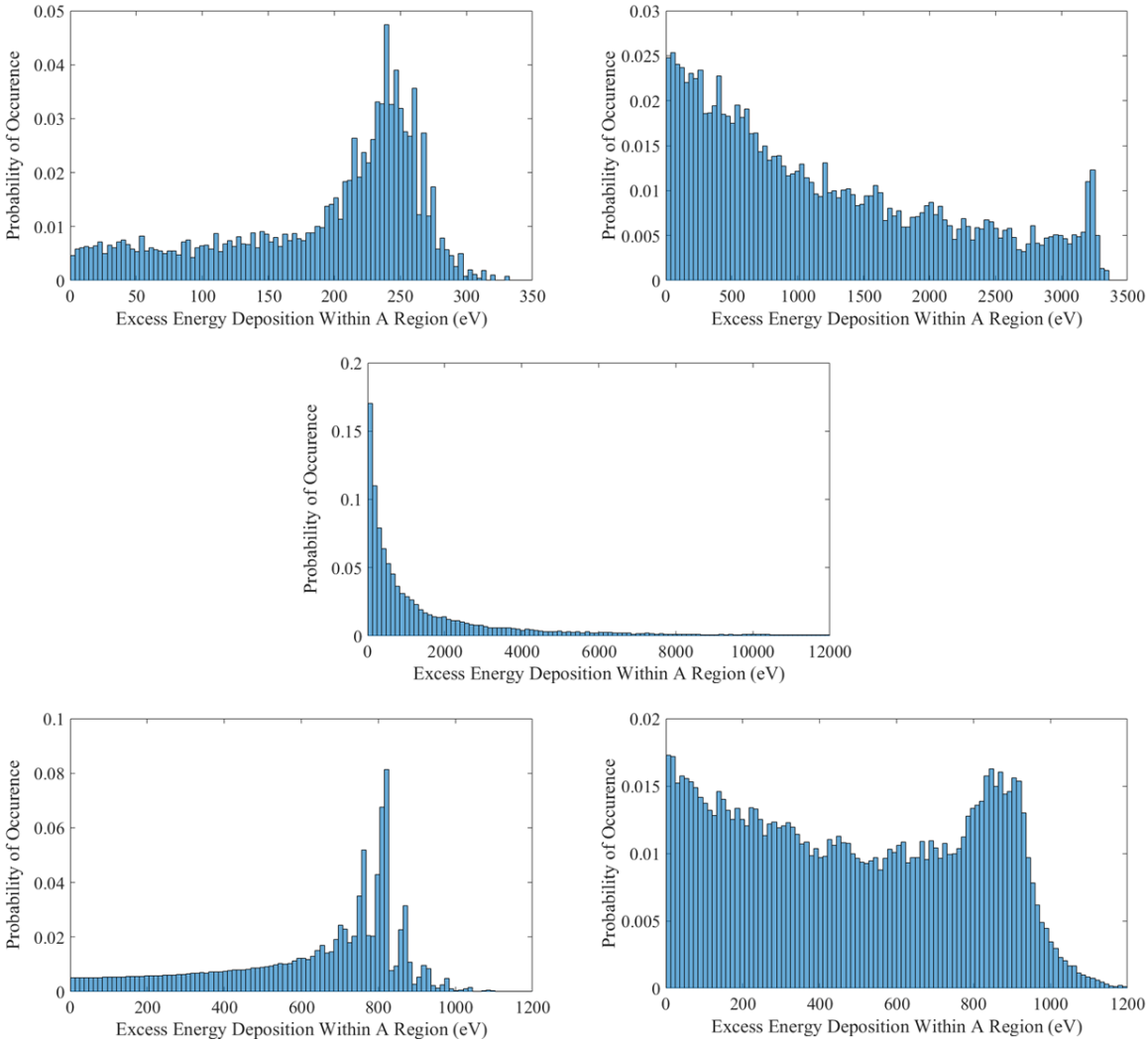

Figure 3.4: Histogram of the distributions of excess energies within the possible nucleation regions. The top plot left plot is the result of 2 keV fluorine particles. The top right plot is the result of 5 keV fluorine particles. The middle plot is the result of 100 keV fluorine particles. The bottom left plot is the result of 1 MeV alpha particles. The bottom right plot is the result of 8 MeV alpha particles. This particular example had a nucleation threshold of 1.75 keV in C_3F_8 at a high superheat 3.1. All histogram were done for 500 tracks except the 8 MeV alpha particles contain only 15 tracks.

where N is the number of molecules, A is the Avogadro number, M is the molecular weight, ρ_v is the vapor density and r_e^3 is the equilibrium bubble radius. With a molecular weight of 188.02 g/mol, 19 nm and 17 nm (see table 3.1) for the equilibrium radii and 56043 g/m^3 and 93204 g/m^3 for the vapor densities, this would yield 1134 molecules and 154 molecules for the high and low superheat conditions, respectively. Using the ideal gas law the relation between kinetic energy and

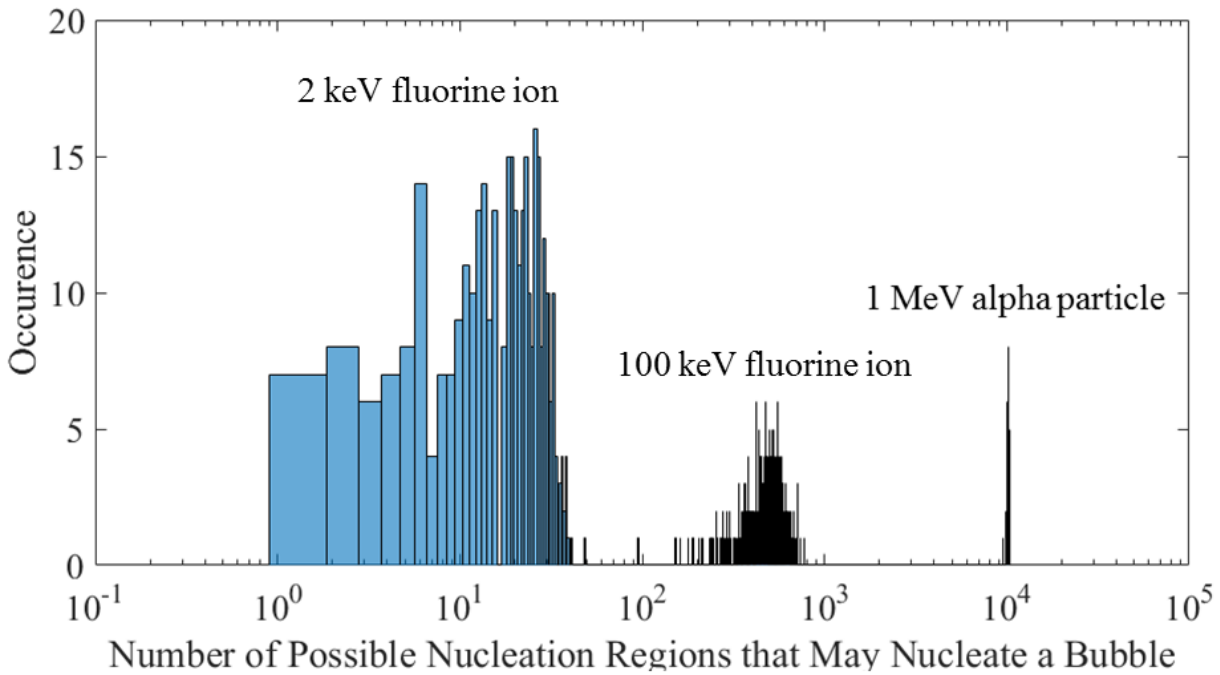

Figure 3.5: Histogram of the number of possible bubbles along particle tracks. The left side of the plot is the result of 2 keV fluorine particles. The middle part of the plot is the result of 100 keV fluorine particles. The right side of the plot is the result of 1 MeV alpha particles. This particular example had a nucleation threshold of 1.75 keV in C_3F_8 at a high superheat 3.1. All components of the histogram were done for 500 tracks.

temperature can be expressed as,

$$E = \frac{3N}{2} k_b T \ . \tag{3.4}$$

As shown in figure 3.4, the range of excess energies within the nucleation regions are of the

Condition	Ideal Gas Relation
High Superheat	0.15 °C/eV
Low Superheat	0.20 °C/eV

Table 3.2: Vapor temperature increase per unit of excess energy using the formula 3.4.

same order of magnitude independent of the particle. In addition, figure 3.5 shows that both the nuclear recoils and the alpha particle have many possible regions that may nucleate a bubble and the total number of regions that may contribute to nucleate bubbles should be greater than one.

Furthermore, the range of excess energies within the regions to form bubbles is large; ranging from hundreds of eV to thousands of eV for the alpha particle. Similarly, from the distribution of excess energies for the nuclear recoils shown in figure 3.4, the range of excess energies is of the same order of magnitude of the alpha particle. Therefore, the increase in vapor temperature for both the nuclear recoils and the alpha particle would be of the same order of magnitude. This is a clear answer to the initial question: the temperature disturbance within a single region alone cannot accurately describe the energy deposition of alpha particles or nuclear recoils. From table 3.2, the vapor temperature increase should be of several tens to hundreds of degrees Celcius. With no experimental data of the vapor temperature of the bubble upon formation, the process of forming a bubble from the energy deposition of a particle and determining the characteristics of the bubbble, i.e. the vapor temperature, the vapor pressure, the size, the interface thickness, etc., should be studied further to develop a more appropriate model. The C_3F_8 molecule is shown in 3.6. It is observed that the center of mass lies outside of the carbon chain. This indicates that elastic recoils could induce rotations which complicates the conversion of energy to temperature due to the additional degrees of freedom. Additionally, and maybe more importantly, these studies should also include the merging of multiple growing bubbles, because what is observed in PICO is the final, single, bubble, which is the product of the merging of all nucleated bubbles along the track of an incoming particle.

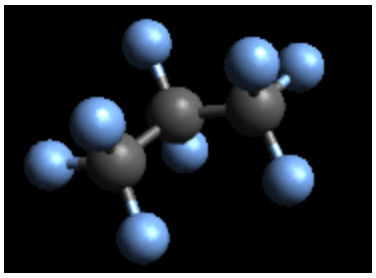

Figure 3.6: Image of the C_3F_8 molecule generated by the Avogadro Software [34]. Carbon atoms are shown in grey and fluorine atoms are shown in blue.

3.2 The Governing Equations

Bubble growth can be modeled as a two-phase flow problem — two phases are in contact separated by a moving boundary and the solution is the time evolution of both phases and the boundary. To obtain the governing equations, the problem is analyzed with a bubble at equilibrium. It is assumed that a uniform temperature exists at all times inside the vapor phase and the liquid phase extends far enough that the temperature gradients far away are negligible in comparison to those at the interface. The uniformity of the temperature inside the bubble allows the vapor pressure to also be uniform. It will be further assumed that the interface temperature is the same as the vapor temperature. The following developments closely follow that of Wendt [21] and T. G. Leighton [22]. The governing equations arise from continuity equations. Specifically, mass and momentum continuity give rise to the equations of motion of the interface and the energy continuity equation gives rise to the time evolution of the temperature distribution in the liquid. A continuity equation describes the transport of a physical quantity and it is particularly powerful when describing conserved quantities. It expresses that the variation in time of some quantity inside some volume must be equal to the flux of the quantity through the boundaries of the volume and the creation or destruction of the

quantity. A continuity equation can be written in differential form as

$$\frac{\partial \phi}{\partial t} + \nabla \cdot (\phi \vec{u}) + s = 0 \, , \tag{3.5}$$

where ϕ is the conserved quantity, $\vec{u}$ is the velocity field and s is the source or sink term. If the conserved quantity was, for example, the mass, the source or sink term would be the spontaneous creation or destruction of mass. For the conservation of momentum, the conserved quantity is $\rho\vec{u}$, where ρ is the mass density; this quantity is also called the momentum density, and can be written as,

$$\frac{\partial (\rho \vec{u})}{\partial t} + \nabla \cdot (\rho \vec{u} \otimes \vec{u}) + s = 0 \, . \tag{3.6}$$

Careful attention must be paid for the term $\vec{u} \otimes \vec{u}$ that is a tensor product. The equation can be simplified to

$$\rho \frac{\partial \vec{u}}{\partial t} + \vec{u} \frac{\partial \rho}{\partial t} + \vec{u} \otimes \vec{u} \cdot \nabla \rho + \rho \vec{u} \cdot \nabla \vec{u} + (\nabla \cdot \vec{u}) \rho \vec{u} + s = 0 \, , \tag{3.7}$$

$$\rho \left(\frac{\partial \vec{u}}{\partial t} + \vec{u} \cdot \nabla \vec{u} \right) + \vec{u} \left(\frac{\partial \rho}{\partial t} + \nabla \cdot (\rho \vec{u}) \right) + s = 0 \, . \tag{3.8}$$

The terms in the first bracket is the total derivative of $\vec{u}$. The terms in the second bracket is the conservation of mass, where the conserved quantity is ρ the mass density,

$$\frac{\partial \rho}{\partial t} + \nabla \cdot (\rho \vec{u}) = 0 \, . \tag{3.9}$$

There is obviously no creation of mass inside the volume. Therefore, the source term was omitted for this equation, $s = 0$. It is assumed that the liquid is incompressible that implies

$$\frac{\partial \rho}{\partial t} = 0 \, , \tag{3.10}$$

and thus,

$$\nabla \cdot \vec{u} = 0 \, . \tag{3.11}$$

The conservation of momentum can now be written as

$$\rho \frac{d\vec{u}}{dt} = s \, . \tag{3.12}$$

Equation 3.8 has been reduced to $\vec{F} = m\vec{a}$ with just the assumption of incompressibility. Possible forces that may be applied to the surface are pressure, from both the vapor and the liquid, surface stresses and viscosity, respectively. Including these effects, equation 3.12 becomes,

$$\rho \frac{d\vec{u}}{dt} = -\nabla p + \lambda \nabla (\nabla \cdot \vec{u}) + \mu \nabla^2 \vec{u} \, . \tag{3.13}$$

The term $-\nabla p$ is the pressure difference from inside the bubble and outside, i.e. the vapor and the liquid respectively. The functions λ and μ describe the surface stresses and viscosity respectively. Equation 3.13 can be simplified since the liquid was assumed to be incompressible $\nabla \cdot \vec{u} = 0$. Spherical coordinates are chosen as bubble growth is assumed to be radial. The radial motion

would yield the following equation

$$\nabla \cdot \vec{u} = \frac{1}{r^2}\frac{\partial}{\partial r}(r^2 u_r) = 0 \ , \tag{3.14}$$

which implies that

$$r^2 u_r = constant \ , \tag{3.15}$$

and must still be true at the interface which is at position R

$$r^2 u_r = R^2 \frac{dR}{dt} \tag{3.16}$$

$$u_r = \frac{R^2}{r^2}\frac{dR}{dt} \ . \tag{3.17}$$

It is possible to rewrite $\vec{u}$ as a gradient of a potential Φ

$$\Phi = -\frac{R^2}{r}\frac{dR}{dt} \ , \tag{3.18}$$

and in this case the Laplacian would be equal to zero in equation 3.13, therefore the viscosity, at first glance, does not not affect the equation of motion. The boundary conditions at the interface will recover the dependance on the viscosity. A stress vector can be defined as the following

$$\vec{P} = P_r \hat{r} + P_\theta \hat{\theta} + P_\phi \hat{\phi} \tag{3.19}$$

$$\vec{P} = \vec{P}_L + 2\mu\vec{\varepsilon} \tag{3.20}$$

$$\vec{P}_L = -P_L \hat{r} \ . \tag{3.21}$$

The radial stress, P_r can be defined as,

$$P_r = -P_L + 2\mu\varepsilon_r \ . \tag{3.22}$$

The radial strain, ε_r is given by $d\vec{u}/dr$ and therefore

$$P_r = P_L - 2\mu\left(2\frac{R^2}{r^3}\frac{dR}{dt}\right) \ . \tag{3.23}$$

Going back to the equation of motion from equation 3.13 and isolating the radial component would give

$$\rho\left(\frac{\partial\vec{u}}{\partial t} + u_r\frac{\partial u_r}{\partial r}\right) = -\frac{\partial p}{\partial r} \ . \tag{3.24}$$

If equation 3.24 is integrated over r from the interface to infinity and keeping in mind that $\vec{u} = \nabla\Phi$, this would yield

$$\left.\frac{\partial\Phi}{\partial t}\right|_R + \left.\frac{u_r^2}{2}\right|_R = P_\infty - P_R \ , \tag{3.25}$$

where P_R is P_r from equation 3.23 but evaluated at the interface $r = R$. Using the relations 3.17 and 3.18 the left-hand side becomes

$$-\frac{1}{r}\frac{\partial}{\partial t}\left(R^2\frac{dR}{dt}\right)\bigg|_R + \left.\frac{R^4}{2r^4}\frac{dR}{dt}\right|_R = P_\infty - P_R \tag{3.26}$$

$$-\frac{3}{2}\left(\frac{dR}{dt}\right)^2 - R\frac{d^2R}{dt^2} = P_\infty - P_L + \frac{4\mu}{R}\frac{dR}{dt} \ . \tag{3.27}$$

The liquid pressure at the interface can be rewritten in terms of the vapor pressure and the surface tension in the following manner

$$P_L = P_v - \frac{2\sigma}{R} \tag{3.28}$$

$$-\frac{3}{2}\left(\frac{dR}{dt}\right)^2 - R\frac{d^2R}{dt^2} = P_\infty - P_v + \frac{2\sigma}{R} + \frac{4\mu}{R}\frac{dR}{dt} \tag{3.29}$$

$$\frac{d^2R}{dt^2} = \frac{P_v - P_\infty}{\rho R} - \frac{2\sigma}{\rho R^2} - \frac{4\mu}{\rho R^2}\frac{dR}{dt} - \frac{3}{2\rho R}\left(\frac{dR}{dt}\right)^2 , \tag{3.30}$$

where equation 3.30 is the Navier-Stokes equation, the first governing equation for the growth of a bubble.

The vapor pressure and surface tension are both functions of the temperature at the interface, therefore the energy continuity equation is required to know how the temperature at the interface evolves with time. The continuity equation for energy can be written as

$$\frac{\partial \rho C_p T}{\partial t} + \nabla \cdot \vec{j} = S , \tag{3.31}$$

where C_p is the heat capacity, $\vec{j}$ is the total flux due to diffusion and advection, $\vec{j} = \vec{j}_{\text{diffusion}} + \vec{j}_{\text{advection}}$ and S is sources or sinks of energy. Since energy is conserved, $S = 0$. Diffusion can be summarized by Fick's law and advection is due to the motion of the fluid,

$$\vec{j}_{\text{diffusion}} = -k\nabla T , \tag{3.32}$$

$$\vec{j}_{\text{advection}} = \vec{u}T , \tag{3.33}$$

where k is the thermal conductivity. The continuity equation 3.31 can be completed,

$$\frac{\partial \rho C_p T}{\partial t} + \nabla \cdot (-k\nabla T + \vec{u}T) = 0 \, . \tag{3.34}$$

Assuming spherical symmetry and that neither C_p or k vary in time or space,

$$\frac{\partial T}{\partial t} + \frac{1}{r^2}\frac{\partial}{\partial r}\left(r^2\left(-\alpha\frac{\partial T}{\partial r}\right)\right) + \frac{1}{r^2}\frac{\partial}{\partial r}\left(r^2(u_r T)\right) = 0 \, , \tag{3.35}$$

where α is the thermal diffusivity and is defined as $\frac{k}{C_p\rho}$. The assumption that C_p and k are constant is only valid for small temperature variations in space and time. This yields the final governing equation, the heat equation:

$$\frac{\partial T}{\partial t} + u_r\frac{\partial T}{\partial r} = \alpha\left(\frac{\partial^2 T}{\partial r^2} + \frac{2}{r}\frac{\partial T}{\partial r}\right) . \tag{3.36}$$

Now that the two governing equations to describe the two-phase flow problem have been derived, the numerical method to solve the equations will be presented next.

3.2.1 Solving the Coupled Equations

This section will closely follow the papers of A. J. Robinson [19], T. Kajishima and K. Taira [20] and J. Went [21]. The time-stepping requirements to solve both equations simultaneously can be adequately achieved with a 4^{th} order Runge-Kutta method. As discussed earlier, bubble growth is a two-phase flow problem of superheated liquid and vapour separated by a moving interface. The process of nucleation and relevant calculations are presented in appendix A. To begin the calcula-

tion, the temperature of the bubble is slightly perturbed from equilibrium. It is assumed, without proof, that the temperature within the bubble is uniform throughout the growth [17][19][22]. For this to be true, heat must diffuse from the interface to the center of the bubble faster than the bubble can grow. The interface for the problem is considered to be ideal, i.e. zero-thickness but non-zero thermodynamic properties as described in appendix A. In addition, the temperature of the vapor is considered to be the temperature at the interface. To solve the heat equation and the Navier-Stokes equation, they are rendered dimensionless in space to avoid integrating over an infinite range. The spatial domain is reduced to a finite length with a distant point, R_∞, where the temperature gradients are small and the temperature remains constant. To render the Navier-Stokes equation dimensionless the spatial variable is rewritten as,

$$r = R(t) + \delta f(\eta) \ , \tag{3.37}$$

where $R(t)$ is the position of the bubble's interface, η, $0 \leq \eta \leq 1$, is a dimensionless variable, δ parametrises the distance between the boundaries and it is defined as,

$$\delta = R_\infty - R(t) \ . \tag{3.38}$$

The function $f(\eta)$ is a clustering function. For the purpose of bubble growth, the function will cluster points at the interface. The following change of variable from $r \rightarrow \eta$ is required. The

spatial derivatives become

$$\frac{\partial T}{\partial r} = \frac{\partial T}{\partial \eta}\frac{\partial \eta}{\partial r} \,, \tag{3.39}$$

$$\frac{\partial^2 T}{\partial r^2} = \frac{\partial}{\partial \eta}\left(\frac{\partial T}{\partial \eta}\frac{\partial \eta}{\partial r}\right)\frac{\partial \eta}{\partial r} \,, \tag{3.40}$$

$$\frac{\partial^2 T}{\partial r^2} = \frac{\partial^2 T}{\partial \eta^2}\left(\frac{\partial \eta}{\partial r}\right)^2 + \frac{\partial T}{\partial \eta}\frac{\partial^2 \eta}{\partial r^2} \,. \tag{3.41}$$

Choosing a function that clusters the spatial points increases the performance of the calculation. An exponential grid clustering was chosen for this thesis, giving,

$$f(\eta) = \frac{e^{\beta\eta} - 1}{e^{\beta} - 1} \,, \tag{3.42}$$

$$\frac{\partial \eta}{\partial r} = \frac{1}{\beta}\frac{e^{\beta} - 1}{\delta}e^{-\beta\eta} \,, \tag{3.43}$$

$$\frac{\partial^2 \eta}{\partial r^2} = -\frac{1}{\beta}\left(\frac{e^{\beta} - 1}{\delta}\right)^2 e^{-2\beta\eta} \,, \tag{3.44}$$

where β is a constant that is chosen to adequately cluster the points at the interface. The partial time derivative of the heat equation needs to become a total derivative, as shown below,

$$\frac{dT}{dt} = \frac{\partial T}{\partial r}\frac{dr}{dt} + \frac{\partial T}{\partial t} \,, \tag{3.45}$$

$$\frac{dr}{dt} = -f(\eta)\dot{R} + \dot{R} \,, \tag{3.46}$$

$$\frac{dT}{dt} = \frac{1}{\delta}\frac{\partial T}{\partial \eta}(\dot{R} - f(\eta)\dot{R}) + \frac{\partial T}{\partial t} \,. \tag{3.47}$$

Combining equations 3.36, 3.39, 3.41 and 3.47 yields,

$$\frac{dT}{dt} + a\frac{\partial T}{\partial \eta} + b\frac{\partial^2 T}{\partial \eta^2} = 0 \,, \tag{3.48}$$

where

$$a = \frac{\partial \eta}{\partial r}\left(\dot{R}(\eta-1) - \frac{2\alpha}{f(\eta)\delta + R} + \left(\frac{R}{f(\eta)\delta + R}\right)^2 \dot{R}\right) - \alpha\frac{\partial^2 \eta}{\partial r^2} \ , \tag{3.49}$$

$$b = -\alpha\left(\frac{\partial \eta}{\partial r}\right)^2 . \tag{3.50}$$

Equation 3.48 is well suited to have the derivatives replaced with any particular finite difference scheme. The derivation of a finite difference scheme is shown in detail in appendix B. There are two boundary conditions: the first is related to the heat transfer at the bubble interface and the second is the temperature at the distant point that must remain constant. The initial conditions are: the perturbed vapor temperature inside the bubble and the constant initial temperature distribution outside the bubble. These initial conditions and boundary conditions can be summarized as

$$T(R,0) = T_{sat}(\infty,0) + T_{dist} \ , \tag{3.51}$$

$$T(r,0) = T_\infty \ , \tag{3.52}$$

$$T(R_\infty,t) = T_\infty \text{ and} \tag{3.53}$$

$$\rho_v h_{fg}\frac{dR}{dt} + h_{fg}\frac{R}{3}\frac{d\rho_v}{dt} = \frac{1}{4\pi R^2}\int_S k_l \frac{\partial T}{\partial \eta}\bigg|_R dA \ . \tag{3.54}$$

Equation 3.54 is the conservation of energy and mass at the interface. The following must be true

$$\frac{dm_v}{dt}h_v + \frac{dm_l}{dt}h_l + q_{v,out} - q_{l,in} = 0 \ . \tag{3.55}$$

From the assumption that the temperature is uniform inside the bubble, $q_{v,out} = 0$ and from mass continuity the mass flux in must be equal to the mass flux out, such that

$$\frac{dm_v}{dt} + \frac{dm_l}{dt} = 0 \, . \tag{3.56}$$

Equation 3.55 can therefore be re-written and completed as follows,

$$-h_{fg}\frac{dm_v}{dt} + \int_A k_l \left(\frac{\partial T}{\partial r}\right) = 0 \, , \tag{3.57}$$

$$h_{fg}\left(V\frac{d\rho_v}{dt} + \rho A\frac{dR}{dt}\right) = \int_A k_l \left(\frac{\partial T}{\partial r}\right) \, , \tag{3.58}$$

which yields equation 3.54. The method used to solve the heat equation was to replace derivatives with finite differences, e.g. backward difference in time and a central difference in space. To simplify the notation, subscripts j will refer to space and superscripts n will refer to time,

$$\left.\frac{dT}{dt}\right|_{\eta,t} = \frac{1}{\delta t}[T_j^n - T_j^{n-1}] + O(\delta t) \, , \tag{3.59}$$

$$\left.\frac{\partial^2 T}{\partial \eta^2}\right|_{\eta,t} = \frac{1}{(\delta x)^2}[T_{j+1}^n - 2T_j^n + T_{j-1}^n] + O(\delta x)^2 \, , \tag{3.60}$$

$$\left.\frac{\partial T}{\partial \eta}\right|_{\eta,t} = \frac{1}{2\delta x}[T_{j+1}^n - T_{j-1}^n] + O(\delta x) \, . \tag{3.61}$$

Substituting equations 3.59 to 3.61 back into equation 3.48 and using equations 3.49 and 3.50 gives the following set of equations,

$$T_j^{n-1} - \alpha_j^n T_v^n = \lambda_j^n T_{j+1}^n + \beta_j^n T_j^n \; for \; j = 2 \; , \tag{3.62}$$

$$T_j^{n-1} = \lambda_j^n T_{j+1}^n + \beta_j^n T_j^n + \alpha_j^n T_{j-1}^n \; for \; 3 \leq j \leq END - 2 \; , \tag{3.63}$$

$$T_j^{n-1} - \lambda_j^n T_\infty^n = \beta_j^n T_j^n + \alpha_j^n T_{j-1}^n \; for \; j = END - 1 \; , \tag{3.64}$$

$$\lambda_j^n = \frac{b_j^n \delta t}{(\delta x)^2} + \frac{a_j^n \delta t}{2\delta x} \; , \tag{3.65}$$

$$\beta_j^n = 1 - \frac{2 b_j^n \delta t}{(\delta x)^2} \; , \tag{3.66}$$

$$\alpha_j^n = \frac{b_j^n \delta t}{(\delta x)^2} - \frac{a_j^n \delta t}{2\delta x} \; . \tag{3.67}$$

The word "END" is used to describe the last grid point. The constants α and β are not to be confused with those previously defined as they are specific to this section only. This method suffers from being highly unstable and it imposes very stringent conditions on δt and δx, as will be shown later.

This representation is now adequate and can be used to solve the coupled differential equations 3.30 and 3.36. Below we show the algorithm to solve the problem. Three functions are required that contain all the information for the bubble growth curves: the interface temperature, the interface

velocity and the interface position (i.e. the radius of the bubble in our scheme),

$$y_1 = T_v \ , \tag{3.68}$$

$$y_2 = R(t) \ , \tag{3.69}$$

$$y_3 = \frac{dR(t)}{dt} \ , \tag{3.70}$$

which can be rearranged to form a set of equations that are well suited for a Runge-Kutta integration:

$$\frac{d(y_1)}{dt} = \frac{dT_v}{dt} \ , \tag{3.71}$$

$$\frac{d(y_2)}{dt} = \frac{dR(t)}{dt} \ , \tag{3.72}$$

$$\frac{d(y_3)}{dt} = \frac{d^2R(t)}{dt^2} \ . \tag{3.73}$$

Equation 3.71 must be rearranged because the evolution of the vapor temperature is unknown. The NIST property data base supplies the thermodynamic data of C_3F_8 [35]. The data includes the variation of the vapor density with temperature. It is possible to rearrange the boundary condition 3.54 and use the chain rule, $\frac{d\rho_v}{dt} = \frac{d\rho}{dT_v}\frac{dT_v}{dt}$, to isolate $\frac{dT_v}{dt}$. The heat equation is then solved to find the temperature gradient at the interface. The temperature at the interface is used to find the vapor pressure inside the bubble, which is finally used to advance one step in time that, from the Navier-Stokes equation, gives the position, velocity and acceleration of the interface. The iteration is repeated until the desired size of the bubble is achieved.

3.2.2 Bubble Growth in Superheated Water

The numerical procedure that was previously described in section 3.2.1 is very similar to both H. S. Lee and H. Merte [17] and A. J. Robinson [19]. In order to verify our method, a calculation of bubble growth in superheated water was performed in order to compare with their results. The results obtained by employing our method are shown on the bottom of figures 3.7, 3.8 and 3.9 which consistently reproduce the results of H. S. Lee and H. Merte presented in the top plot of the figures. Minor discrepancies arise at the beginning of the interface velocity curves, at the beginning of the interface acceleration curve and with the peak interface acceleration. H. S. Lee and H. Merte present various bubble growth curves corresponding to three temperature disturbances, 10^{-9} °C, 10^{-5} °C and 10^{-1} °C, and two superheat conditions, a high superheat of 36 °C and a low superheat of 3.1 °C; all curves have arrows pointing to the correct y-axis. A 3.1 °C superheat and temperature disturbances of 10^{-9} °C and 10^{-12} °C were chosen due to visual clarity. The bubble growth with these temperature disturbances showed an important characteristic: there is a delay before the perceptible growth of the bubble. Our method also shows this characteristic and reproduces it as shown in the bottom plot of figure 3.7. Two temperature disturbances were chosen. Initially, it was thought that the temperature disturbance could describe the energy deposition of incoming particles. Even though it was shown in section 3.1 that temperature disturbances alone cannot describe the energy deposition, the delay can still be useful and this will be discussed later in section 3.3.

The first discrepancy, the non-flat beginning of the interface velocity for the current numerical solution can be explained by inspecting the Navier-Stokes equation 3.30. It reveals that an increase

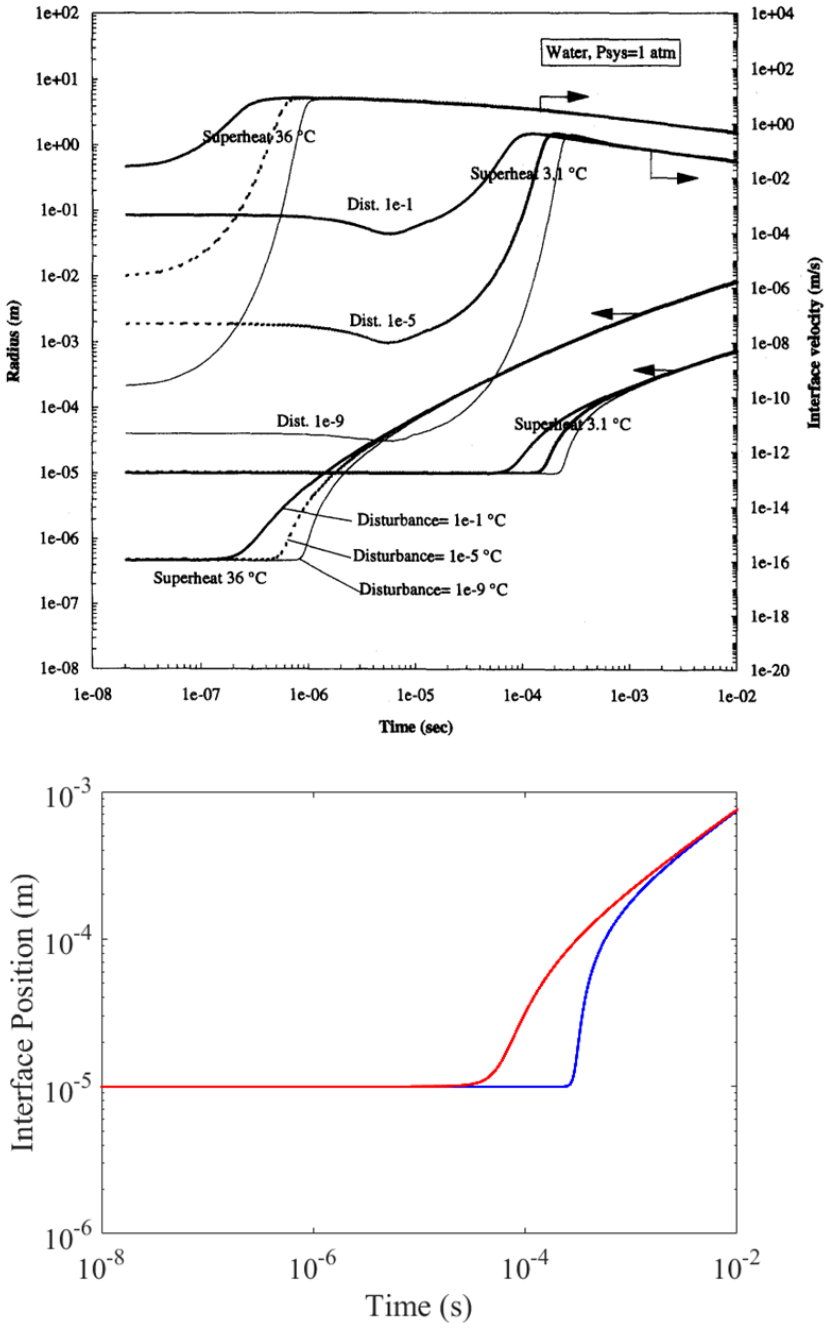

Figure 3.7: The top plot shows the results of H. Merte and H. S. Lee [17]. The bottom plot shows the current numerical solution of the growth of a bubble in superheated water. The current numerical solution reproduces the interface position curve with superheats of 3.1°C and a temperature disturbance of 10^{-9} °C.

in vapor temperature at the interface must be accompanied by a decrease in surface tension and an increase in vapor pressure, thus, the acceleration cannot be zero [35]. This implies that the

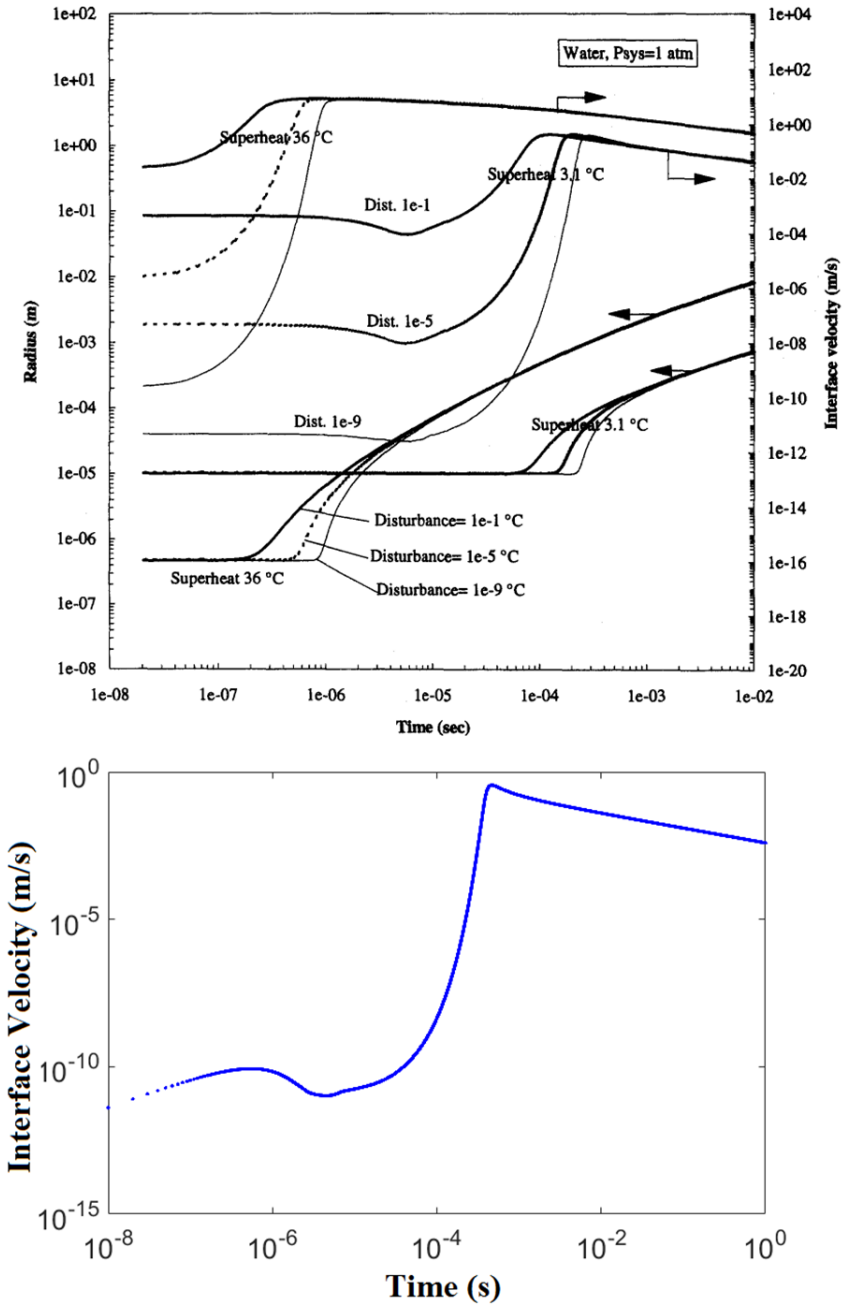

Figure 3.8: The top plot shows the results of H. Merte and H. S. Lee [17]. The bottom plot shows the current numerical solution of the growth of a bubble in superheated water. The current numerical solution reproduces the interface velocity curve with superheats of 3.1°C and a temperature disturbance of 10^{-9} °C.

interface velocity cannot be flat.

The second and third discrepancies are the presence of oscillations and the difference in peak

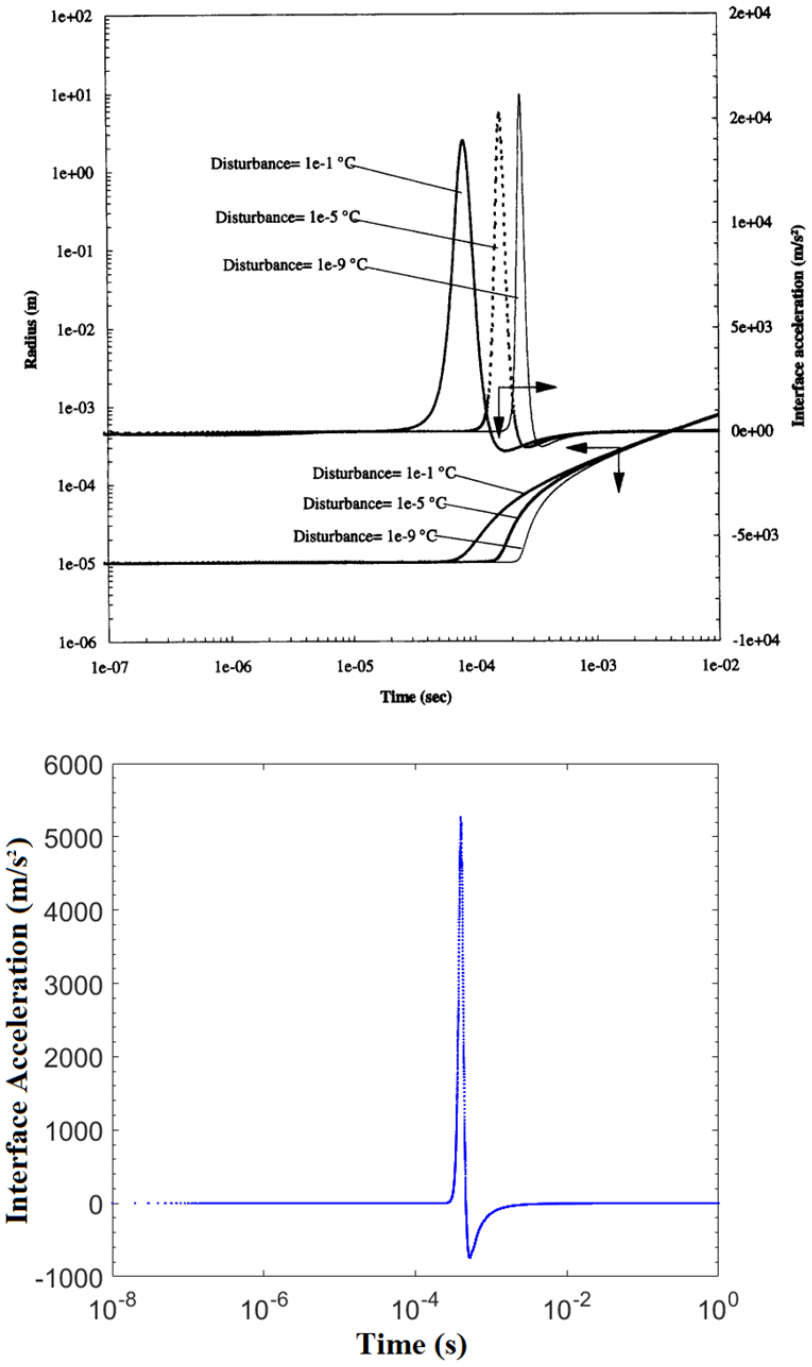

Figure 3.9: The top plot shows the results of H. S. Lee and H. Merte [17]. The bottom plot shows the current numerical solution of the growth of a bubble in superheated water. The current numerical solution attempts to reproduce the interface acceleration curve with superheats of 3.1°C and a temperature disturbance of 10^{-9} °C.

interface acceleraion. They are most likely related to numerical parameters, i.e the time step and spatial step, and to the convergence of the numerical solution. The oscillations at the beginning

of the interface acceleration could be, in part, an effect of the finite differences used to transform the derivatives. Experimental data is required to resolve the discrepancies. Another explanation might reside in the temperature disturbances themselves. As discussed at the beginning of the chapter, many types of perturbations from equilibrium exist. There is no apparent reason for the physics of bubble formation to only depend on one of the possible types of perturbations. Most likely, the appropriate perturbation would be a combination of all the types of perturbations. One example perturbation was a change in size. If the size of the bubble is slightly increased, this would lead in a decrease in pressure and, therefore, a decrease of the interface acceleration in the beginning of the growth. In regards to the numerical convergence of the solution, the solution to a calculation cannot depend on the method nor can it depend on the numerical parameters, such as spatial resolution or time resolution. A converged numerical solution satisfies the following condition: the variation of the numerical solution is within a degree of tolerance when varying the numerical parameters, i.e. the time step and spatial step. In an ordinary situation, the numerical solution is found with coarse parameters and refined until the condition is satisfied. The initial oscillations of the interface acceleration are due to the temperature gradient at the interface and to the numerical parameters of the calculation: the time step and spatial resolution. If the time step is too coarse, the heat transfer will be too large without the appropriate affects of advection. If the spatial resolution is too coarse, the temperature gradient is either underestimated or overestimated and leads to an unstable, oscillatory, calculation. Adequately choosing a function to cluster points early in the bubble growth and a function to cluster points close to the interface is important. Both clustering functions that were chosen are exponential functions for their ease of use.

3.2.3 Bubble Growth in C_3F_8

The dynamics of bubble growth is affected by three parameters: the temperature, the working pressure and the perturbation. Furthermore, the numerical calculation is affected by two additional parameters: the time step and spatial resolution. These two numerical parameters affect the convergence of the solution as discussed in previous sections. In view of the fact that PICO utilizes detectors where the threshold of nucleation is the parameter of importance, all results will be presented at iso-threshold that restricts the freedom to choose the temperature and working pressure. As discussed in section 3.1, this gives rise to the possibility of a high and low superheat detector that would correspond to the conditions described in table 3.1. Additionally, the temperature disturbances of 10^{-1} °C and 10^{-12} °C were chosen to be compared with the work of H. S. Lee and H. Merte [17]. These are also the maximum and minimum disturbances that yielded a stable converging numerical solution. It was observed during the investigation of convergence, i.e. while varying the numerical parameters, the peak acceleration would occur earlier or later in time and its amplitude would change. Figure 3.10 presents how the solution varies with respect to the change in the number of grid points for the grid clustering. It was observed that if the time step is chosen too large the solution diverges, i.e. the solution oscillates with increasing amplitude. If the time step is smaller than a critical value, the solution does not change and the overall shape remains the same.

It should be noted that the spatial step is a function of two values, the grid clustering coefficient

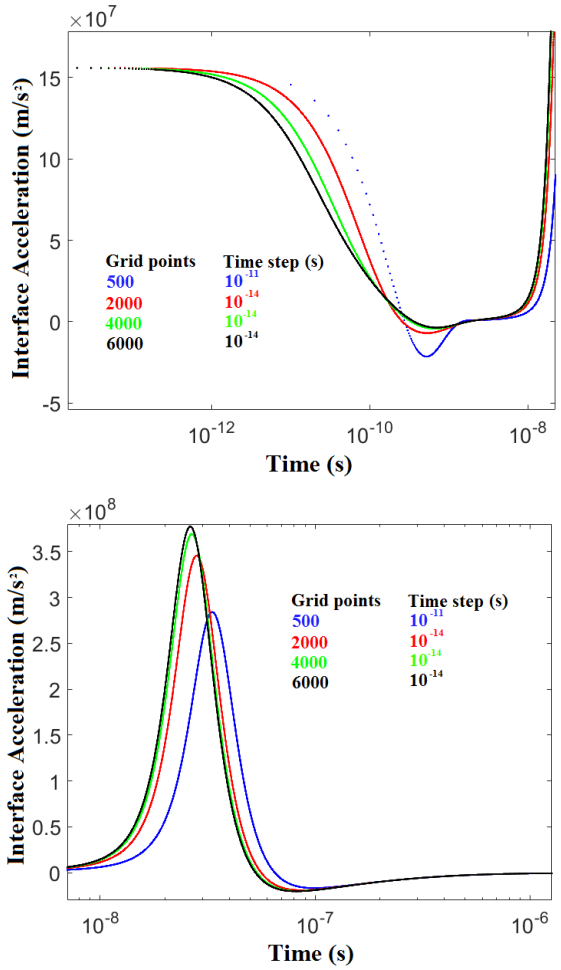

Figure 3.10: The plot shows the convergence of the numerical calculation for increasing number of grid point and finer time steps. Two sections of the curve are presented, the top plot is the very early stage of bubble growth and at the bottom is the later stage of bubble growth. This curve shows the result of the calculation for C_3F_8 in a high superheat condition.

and the number of points. The spatial distribution was chosen to be the following

$$r = f(\eta)\delta + R(t) \,, \tag{3.74}$$

$$f(\eta) = \frac{e^{\alpha\eta} - 1}{e^{\alpha} - 1} \,, \tag{3.75}$$

$$\delta = R_{\infty} - R(t) \,, \tag{3.76}$$

where η is a variable whose range is $[0,1]$ and equally spaced. The function $f(\eta)$ has values

between $[0,1]$ and its purpose is to cluster the spatial points r near the interface at $R(t)$. δ is the length of space outside of the bubble. The far point, R_∞, is chosen such that the temperature gradients at that point, or near that point, are negligible compared to those near the interface. In other words, the temperature at the far point should remain approximately constant. The clustering parameter, α, controls the density of points at the interface. The spatial step is then a function of the number of grid points, the length of space, the clustering parameter and of time. The clustering parameter has a very large effect for small changes. A starting value of 12 was found by trial and error and subsequently the number of points for η was varied instead until convergence was achieved. The far point was, also, chosen by trial and error to be further than 0.5 m in both water and C_3F_8. For reference, whenever a calculation is performed, a convergence check is made to assure it may be used for comparison later. The growth of a bubble in C_3F_8 will be separated in stages and the effects of the detector conditions and the temperature disturbances will be examined.

3.2.4 Stages of Bubble Growth

The growth of a bubble can be separated into three stages: the surface tension controlled stage, the transition stage and inertia and heat transfer controlled stage. Each one of these stages has its own relationship with the physical parameters of the Navier-Stokes equation 3.30. These stages are more readily distinguishable from both the interface velocity and the interface temperature depicted in figure 3.11.

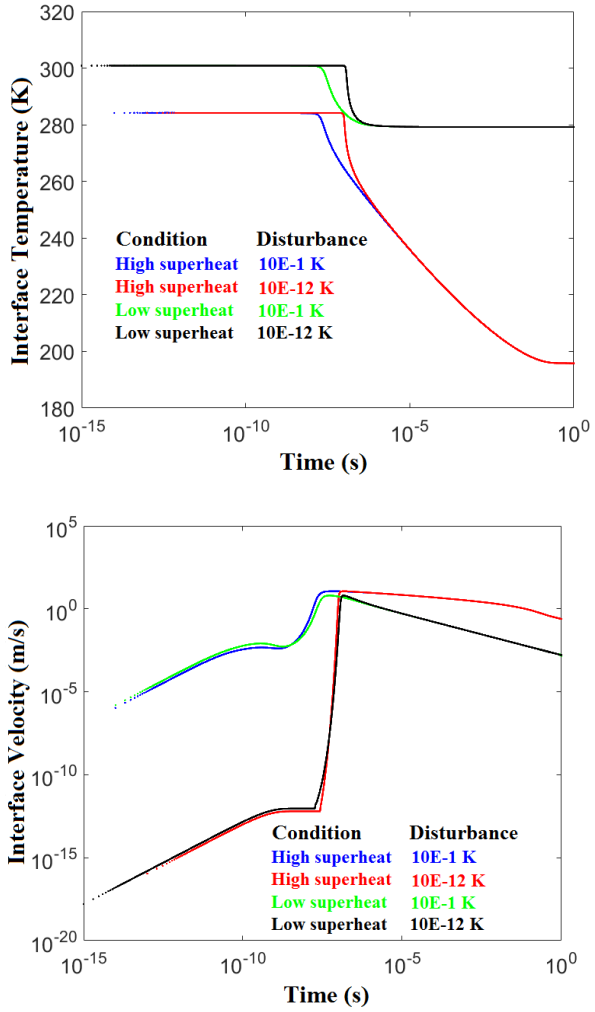

Figure 3.11: The top plot shows the interface temperature and the bottom plot shows the interface velocity for the high and low superheat detector conditions at 1.75 keV threshold as shown in table 3.1 in C_3F_8. For each detector condition two temperature disturbances are shown: a disturbance of 10^{-1} °C and a disturbance of 10^{-12} °C [17].

Surface Tension Controlled Growth

The surface tension stage takes place from the very beginning of the bubble's growth until noticeable change in the bubble's radius. This stage is usually characterized by very slow changes in temperature, pressure and radius. The surface tension term is the component of the Navier-Stoke equation that contains the surface tension, $2\sigma/R^2$. The surface tension, σ is a function of the

temperature and is taken at the interface. The magnitude of the surface tension term increases for bubbles with a smaller initial radius. During the very early moments after the bubble growth is initiated by the temperature disturbance, the interface velocity and acceleration remain small compared to their respective peaks. For a very brief period, heat is transferred to the liquid from the vapor. This transfer of heat induces large accelerations but it quickly decays. Even though the acceleration is large early for a short period of time, the Navier-Stoke equation reduces to $P_v - P_\infty \approx 2\sigma/R$. Therefore, since P_∞ is constant, an increase in radius must be accompanied by a decrease in P_v and, thus, a decrease in temperature as shown figure 3.11. The temperature drop at the interface increases the temperature gradient between the interface and the liquid, thus increasing the heat transfer into the bubble. This heat transfer drives the increase in growth rate, dR/dt. The surface tension controlled stage ends when the change in temperature gradient begins to decrease. This occurs when the surface tension term is of the same order of magnitude that the other contributions as seen in figure 3.13.

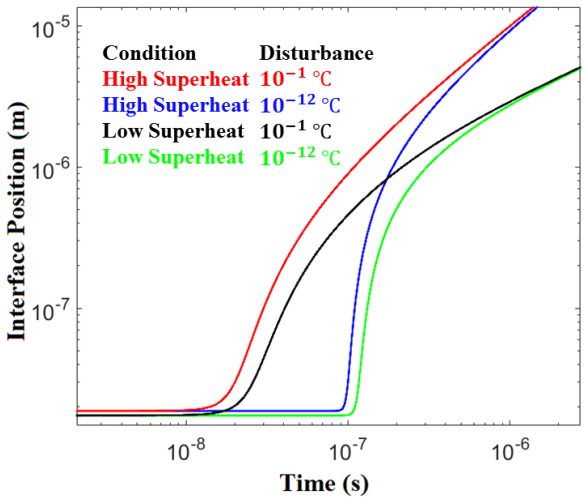

Figure 3.12: The plot shows the evolution of the bubble's radius for a high an low superheat condition 3.1. Each condition shows a high temperature disturbance of 10^{-1} °C and a low temperature disturbance of 10^{-12} °C [17].

Transition Stage and Heat Transfer and Inertia Controlled Stage

The transition stage begins once the surface tension controlled growth ends and lasts until either the heat transfer or inertia dominates the growth. Both these stages have the particularity that they are independent of the cause of the growth. The effects of the temperature disturbance dissipate past the surface tension stage, for example, the interface velocities converge to the same value for both disturbances. The mechanisms involved for this stage are more easily identified from the interface temperature shown in figure 3.11. For a low superheat the return to the saturation temperature is abrupt whilst for a high superheat there is an abrupt fall followed by a slow return to the saturation temperature. The temperature of the interface regulates the pressure of the vapor that is the driving force for the growth in these stages. There are two mechanisms to exchange heat, either by diffusion or advection. Thermal diffusion, or conduction, is the heat transfer due to the thermal conductivity of the interface, and the Fourier law $\dot{q} = -k\nabla T$ describes the process. Advection, or convection, is the heat transfer by the motion of the interface. In the low superheat case, the interface never acquires enough velocity for advection to overcome diffusion whilst for a high superheat the peak velocity is much greater and therefore advection is the main source of heat flux.

3.2.5 Acoustic Signal Generation

The solution to the Navier-Stokes equation is the motion of the interface of the bubble, e.g. the interface position, velocity and acceleration. All of these play a role to determine the output acoustic wave that will ultimately propagate to the piezoelectric transducers. The measured quantity by the

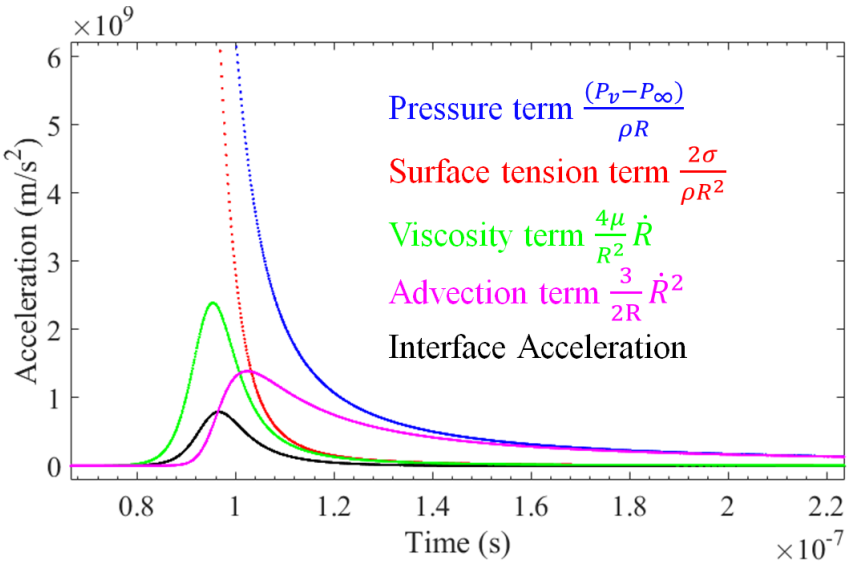

Figure 3.13: Decomposition of the different terms forming the solution to the Navier-Stokes equation as presented in equation 3.30. The interface acceleration from the Navier-Stokes equation 3.30 is shown in black. The pressure term is shown in blue. The surface tension term is shown in red. The viscosity term is shown in green. The advection term is shown in magenta.

piezoelectric transducer is related to the acoustic intensity which this section will develop.

Linearized wave equation

A sound wave is related to the pressure field of the growing bubble which can be retrieved from the mass continuity equation as follows

$$\frac{d\rho}{dt} + \nabla \cdot (\rho \vec{v}) = 0 \,, \tag{3.77}$$

where ρ is assumed to have negligible spatial variation, which allow equation 3.77 to be simplified to

$$\frac{1}{\rho}\frac{d\rho}{dt} + \nabla \cdot \vec{v} = 0 \,. \tag{3.78}$$

The time derivative of equation 3.78 yields

$$\frac{1}{\rho}\frac{d^2\rho}{dt^2} - \frac{1}{\rho^2}\left(\frac{d\rho}{dt}\right)^2 + \nabla \cdot \frac{d\vec{v}}{dt} = 0 \,. \tag{3.79}$$

If the quadratic term is deemed negligible and the flow is inviscid and incompressible, with the use of equation 3.13, with $\vec{v} = \vec{u}$, and where the surface stresses and viscosity are neglected equation 3.79 becomes

$$\frac{1}{\rho}\frac{d^2\rho}{dt^2} - \frac{\nabla^2 P}{\rho_0} = 0 \,, \tag{3.80}$$

where ρ_0 is the density at equilibrium around which the variations were assumed negligible. By using the definition of the bulk modulus at constant entropy, s,

$$B_s = \rho \left.\frac{\partial p}{\partial \rho}\right|_s \,, \tag{3.81}$$

and the definition of the speed of sound in a medium, $c = \sqrt{B_s/\rho}$, it is possible to write

$$\frac{\nabla^2 P}{\rho_0} = \frac{1}{c^2}\frac{d^2 P}{dt^2} \,, \tag{3.82}$$

where solutions are spherical waves. Under the very stringent assumptions of incompressibility and inviscid flow, pressure propagates as spherical waves. The term ”explosive growth” has been used in literature. However, is not apparent from the derived formulas that this is the case so far. The term explosive, or shockwave, is usually used to describe particle velocities that exceed the speed of sound in the fluid. In the case described above, the velocity of the spherical waves would never exceed the speed of sound in the liquid. The shockwave description appears by not

neglecting the quadratic term, the viscosity and the compressibility of liquid. The force balance of equation 3.13 and the mass continuity with the definition of the wave speed are

$$\frac{\partial P}{\partial x} + \rho v \frac{\partial v}{\partial x} + \rho \frac{\partial v}{\partial t} = 0 \,, \tag{3.83}$$

$$\frac{1}{\rho c^2}\frac{\partial P}{\partial t} + \frac{\partial v}{\partial x} + \frac{v}{\rho}\frac{\partial \rho}{\partial x} = 0 \,. \tag{3.84}$$

The two nonlinear terms,

$$\rho v \frac{\partial v}{\partial x} \text{ and} \tag{3.85}$$

$$\frac{v}{\rho}\frac{\partial \rho}{\partial x} \,, \tag{3.86}$$

were neglected previously. The effects on the propagation of the wave will be twofold [22]. First is a convection effect from equation 3.85. If v/c is non-negligible there will be parts of the wave that will propagate as $v+c$. The particle velocities will vary throughout the wave and so the greater the local pressure the greater the velocity of that section of the wave. The second effect arises from physical properties such as bulk modulus and stiffness increasing when the fluid is compressed. This would cause a sinusoidal wave to distort itself. Discontinuities would be created by these distortions, ultimately causing shockwaves. Once the wave propagates through the medium, either as a shockwave or a spherical wave, and reaches a wall (or device) that can absorb the energy of the wave and convert it to a signal, the measured quantity is the acoustic intensity.

Acoustic Intensity

The acoustic intensity is the rate at which energy contained in the wave crosses a unit area perpendicular to its direction of propagation. This can be expressed in the following form

$$I = \frac{1}{t_n - t_0} \int_{t_0}^{t_n} Pv dt \ , \tag{3.87}$$

where P is the radiated pressure and v is the particle velocity. From solving the Navier-Stokes equation and the assumption of an incompressible fluid, both P and v are known. The acoustic pressure of Figure 3.14 shows the acoustic intensities from single bubbles, with temperature disturbances of 10^{-1} °C and 10^{-12} °C.

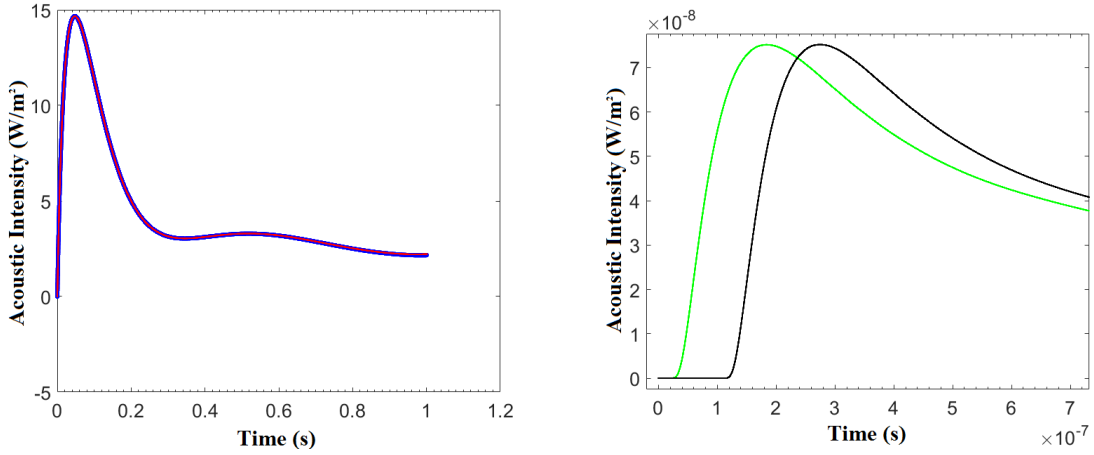

Figure 3.14: Example calculation of the acoustic intensity of a growing bubble in C_3F_8 at high superheat conditions on the left and low superheat conditions of table 3.1. Each condition, separately, shows a high temperature disturbance of 10^{-1} °C in red and green and a low temperature disturbance of 10^{-12} °C in blue and black.

In this case, the acoustic intensities have the shape of a pulse, which is far from a sinusoid. A pulse can be described by an infinite sum of sinusoidal waveforms of varying amplitudes and frequencies through the Fourier transform. For example, a delta-Dirac distribution is an infinite sum of equal

amplitude sinusoidal waveforms of different frequencies. If the measuring device was perfect, it would be able to measure the amplitude of all the different frequencies but this is not the case. To understand the response of a measuring device to a pulse, an illustration will be used. When a guitar string is struck, for example the musical A string, only the A frequency and its harmonics will be heard. This is because energy was transmitted to the string by striking it. The strike itself can be approximated as a delta-Dirac in time for this thought experiment. It was previously stated that the delta-Dirac is represented by an infinite number of sinusoidal waveforms of equal amplitude and different frequencies. If this was the only effect, the energy of the strike would distribute itself amongst all the frequencies and all of them would be heard. This is not the case, only specific frequencies are heard. The cause of this effect is the material's frequency response. The frequency response is a function in the Fourier space that describes how each frequency will be amplified or attenuated. It is a function of the material's physical properties such as length and density. The frequency response is always convoluted to the impulse, or strike as in the example. The guitar's A string will have a frequency response with peaks at the frequency of an A and its harmonics. This situation is the same as when the acoustic pulse hits the piezoelectric transducer. The piezoelectric transducer's frequency response will be convoluted to the acoustic intensity and that is what is measured. Even when the frequency response of the piezoelectric transducer and the impulse cannot be properly de-convoluted, the Fourier transform of the acoustic intensity could potentially give signature peaks which would be regions of interest for the AP. The Fourier transform of the acoustic intensities of figure 3.14 that are the result of growing bubbles with different temperature disturbances are shown in figure 3.15.

Both Fourier transforms for growing bubbles with different temperature disturbances have no dis-

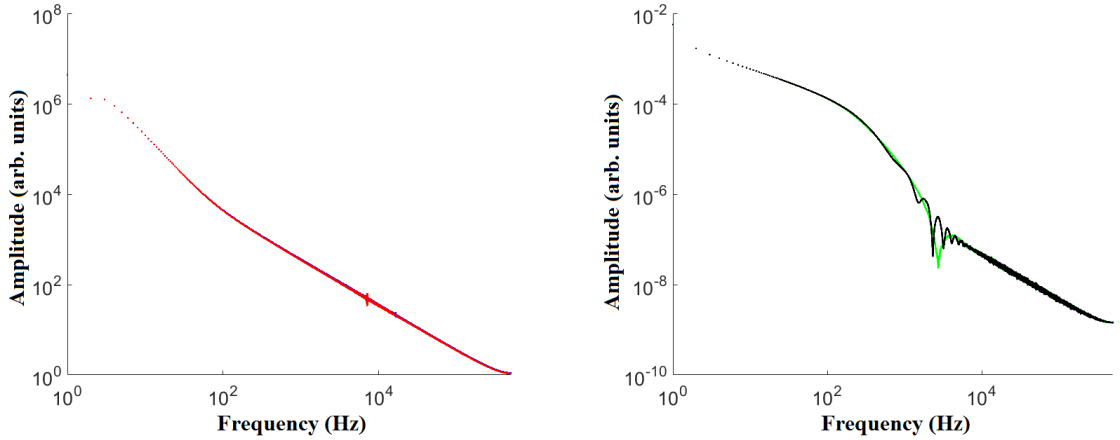

Figure 3.15: Calculation of the Fourier transform of the acoustic intensity produced by the growth of a bubble in C_3F_8 at a high superheat on the left and a low superheat on the right 3.1. Each detector condition shows a high temperature disturbance of 10^{-1} °C in red and green and a low temperature disturbances of 10^{-12} °C in blue and black.

tinguishing features. Apart from the low superheat having oscillating features, these can be explained because the data were interpolated. The features of the interpolating function, being it a spline, would be present in the Fourier transform. As previously mention in section 3.1, the temperature disturbances cannot describe on their own the energy deposition of different types of particles. To describe the differences of the acoustic intensities as observed by PICO, it appears that the merging of many bubbles along the track of an incoming particle must be taken into account [5].

3.3 Optical Observation Of Bubble Growth

Section 3.1 revealed that the tracks of energy deposited by different particles will nucleate multiple bubbles. Once nucleated, they will grow individually until they combine and grow as a unit to form the observed bubble in the PICO detector. Before the merging, as the bubbles are nucleated

the delay prior to perceptible growth can be used to measure the extent of the track and this can potentially be used to distinguish tracks due to nuclear recoils and tracks due to alpha particles. It is possible to foresee a transmittance experiment to observe the track length of an incoming particle. As discussed in section 3.1, an alpha track has a much greater number of possible regions that may nucleate bubbles. Therefore, the total number of nucleated bubbles will always be larger than the nuclear recoils. Assuming that the total distance traveled by the particle, as presented in figure 3.3, is a good first approximation for the length of the track, a 5 keV nuclear recoil would have range of approximately 60 nanometers and a 1 MeV alpha particle would have range of approximately 40 micrometers. The transmittance experiment should be able observe a decrease in light intensity proportional to the length of a track.

Chapter 4

Conclusion

This thesis investigated the possibility of the rate of growth of a bubble, triggered by the energy deposition of an incoming particles, to be used to optically discriminate between two different types particles, i.e. alpha particles and neutron induced fluorine recoils. One of the motivations is the discriminating power of the Acoustic Parameter used by PICO [5]. Further motivation came from the results of numerical calculations of H. S. Lee and H. Merte who showed that temperature perturbations from equilibrium can affect the growth of a bubble in superheated water [17]. One of the effects of their model is an onset delay to perceptible growth. We numerically reproduced this result in superheated water and applied it to superheated C_3F_8. The delay present in water was also present in C_3F_8. While investigating the nature of the temperature perturbations, i.e. the excess energy deposited by a particle within the nucleation region, it was shown that they cannot be used to describe the energy deposition of alpha particles and fluorine ions induced by nuclear recoils. It was shown that these different particles will nucleate many bubbles along their track where

the distribution of excess energies within each of the nucleation regions are all of the same order of magnitude. Each individual bubble nucleated will have approximately the same temperature perturbation and their individual growths will be degenerate. However, it was shown that it is the number of possible nucleation regions along the tracks of different types of particles that is different, leading to the discrimination: an alpha particle will always nucleate more bubbles along its track than a neutron induced nuclear recoil. Therefore, it is the coalescence of many bubbles that form the single growing bubble observed in PICO which is at the heart of the discriminative power of the Acoustic Parameter. In order to describe the acoustic discrimination and possibly the optical one it would be necessary for the model to account for the merging of multiple growing bubbles along the track of the particles and not only the growth of a single bubble. It remains to be realized the implementation of the optical discrimination in this scenario. A proposed follow-up would be to study the formation of bubbles with the use of molecular dynamics software to reconcile how the excess energy within the nucleation region is converted to perturbations from equilibrium, not restricted to only vapor temperature perturbations.

Appendix A

Thermodynamics of Bubble Formation

This appendix follows the ideas of *On the Equilibrium of Heterogeneous Substances* and the theory described in both physical chemistry textbooks [28][29].

A superheated liquid is a liquid whose temperature is greater than the boiling temperature at a certain pressure. The superheat is a term to describe the degree to which a liquid is superheated, it is defined by this relation:

$$T_{sh} = T_l - T_{sat} \ . \tag{A.1}$$

For example, water at 1 atmosphere boils at 100 $^{\circ}C$; liquid water at 101 $^{\circ}C$ it would be superheated and the superheat would be of 1$^{\circ}C$. While superheated, the liquid is in a metastable state where small inputs of energy will cause a phase transition and a bubble will form. The energy required for the phase transition and forming an interface of the correct dimensions to have a bubble at equilibrium can be calculated. This is termed the nucleation energy threshold. An input of energy smaller

than this calculated value would yield a bubble too small and would be incapable of combating the surface tension and would dissolve back into the liquid state. In addition to the nucleation energy threshold, the region in which this energy needs to be deposited may also be calculated. This appendix will overview these calculations.

To start the analysis, the thermodynamic extensive quantities of interest for a system that contains two phases of a pure substance with a separating interface are defined as follows

$$V = V^l + V^v + V^s \ , \tag{A.2}$$

$$U = U^l + U^v + U^s \ , \tag{A.3}$$

$$S = S^l + S^v + S^s \ , \tag{A.4}$$

$$m = m^l + m^v + m^s \ . \tag{A.5}$$

This system is still valid for a liquid containing a vapor bubble, a vapor phase spherically contained by the surface tension of the interface. V defines total volume as the sum of the liquid volume, the vapor volume and the interface volume. Other quantities are the internal energy, U, the entropy, S, and the mass, m. Superscripts represent the phase associated to the quantity, l being liquid, v being vapor and s being the interface. Also, the vapour mass, liquid mass and interface mass will be defined with respective densities, $m^l = \rho^l V^l$, $m^v = \rho^v V^v$ and $m^s = \Gamma A$, where ρ and Γ are volume densities and surface densities respectively. The interface is the only problematic quantity because of how it is defined. Does an interface have a volume? What constitutes the interface? To handle these difficulties the Gibbs model [30] will be used. To depict the interface problem, fig A.1 shows the difference between the model and the actual system that contains an interface. In an actual

system, since the interface is not easily defined it is usually referred to as the interphase region. In this region quantities gradually change from one phase to the other. Gibbs model defines such an interphase region by assuming that this region is a surface of zero volume but other quantities are non-zero, it is usually termed an ideal interface[28][29]. Therefore equation A.2 becomes

$$V = V^l + V^v \,. \tag{A.6}$$

To better understand the methodology of Gibbs, figure A.2 depicts the problem at hand of a bubble at equilibrium. The equilibrium conditions can be written as

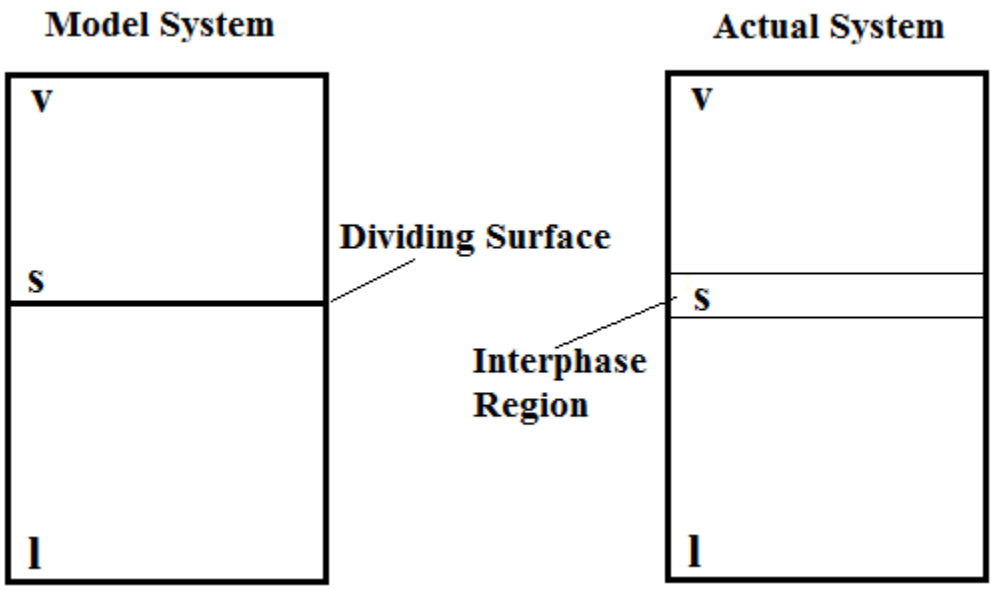

Figure A.1: Representation of the model and the actual systems.

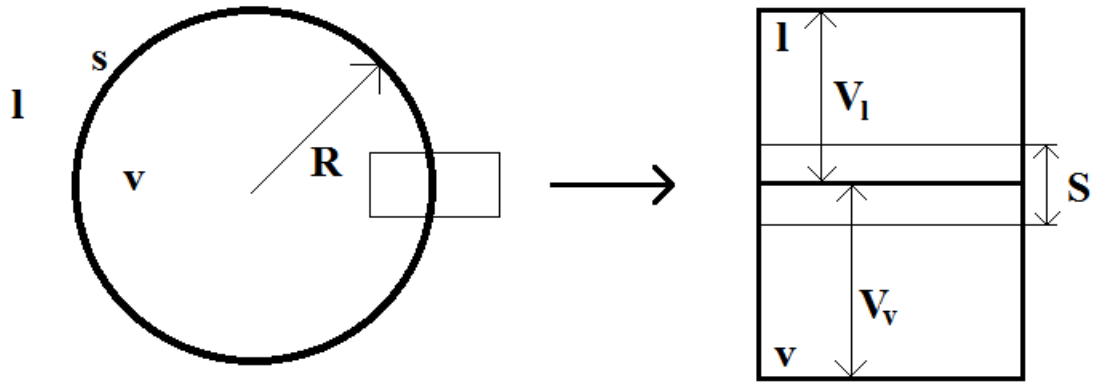

Figure A.2: Depiction of the calculation of the change of mass under the Gibbs model.

$$T^v = T^l \ , \tag{A.7}$$

$$\mu^v = \mu^l = \mu^s \ , \tag{A.8}$$

$$\frac{2\sigma}{r} = P^v - P^l \ . \tag{A.9}$$

The internal energy of the system with the interface is

$$dU = TdS - PdV + \sigma dA + \mu dm \ . \tag{A.10}$$

At this point, this is where Gibbs defines terms called excesses. Imagine a system of volume V filled with one phase. Now imagine the same system of volume V containing two phases and an interface. The difference between the two is the excess. Properties at the interface represent the properties of the interphase region of the actual system. The simplest example to understand these excesses is with the mass. Because in the model the surface has no volume, calculating the total mass from the densities and volumes inserts an error, similar to double counting and the excess

will be the book keeper,

$$V = V^l + V^v \ , \tag{A.11}$$

$$(m^l + m^v + m^s) - m = \varepsilon_m \ , \tag{A.12}$$

$$(\rho^l(V - V^v) + \rho^v V^v + \Gamma A) - \rho^l V = \varepsilon_m \ , \tag{A.13}$$

$$\Gamma A + V^v(\rho^v - \rho^l) = \varepsilon_m \ , \tag{A.14}$$

where m is the total mass (system without the bubble). The excess mass would be ε_m of equation A.14. All excesses would be similarly defined as

$$\varepsilon_m = \Gamma A + V^v(\rho^v - \rho^l) \tag{A.15}$$

$$\varepsilon_u = \Gamma A \frac{U^s}{m} + V^v\left(\frac{U^v}{m}\rho^v - \frac{U^l}{m}\rho^l\right) \tag{A.16}$$

$$\varepsilon_s = \Gamma A \frac{S^s}{m} + V^v\left(\frac{S^v}{m}\rho^v - \frac{S^l}{m}\rho^l\right) \tag{A.17}$$

To simplify notation, subscripts will denote normalization, for example $U_m = \frac{U}{m}$. Excesses are not normalized. For a system of a fixed mass, the change of internal energy would be the difference of the excess internal energy and the internal energy of the excess mass,

$$\Delta U = \varepsilon_u - U_m^l \varepsilon_m \ , \tag{A.18}$$

$$\Delta U = \varepsilon_u + (-TS_m^l + \frac{P^l}{\rho^l} - \mu)\varepsilon_m \ . \tag{A.19}$$

Gibbs defines the excesses with fixed volumes and utilizes the relations for a fixed mass problem. The change of internal energy is known to be the heat input and work done by the outside pressure.

Therefore,

$$\Delta U = Q + P^l \frac{\varepsilon_m}{\rho^l} \ , \tag{A.20}$$

$$\implies Q = \varepsilon_u - T S^l_m \varepsilon_m - \mu \varepsilon_m \ . \tag{A.21}$$

This formulation for Q is not very useful as there are no surface terms and ε_m is not a measurable term. Since thermodynamic quantities are true for all components of the system, at the interface the quantities would be

$$U^s = T S^s + \mu m^s + \sigma A \ , \tag{A.22}$$

where equation A.22 has an extra term σA which represents the surface energy. U^s, S^s and m^s can be replaced to give

$$\varepsilon_u - V^v(U^v_m \rho^v - U^l_m \rho^l) = T(\varepsilon_s - V^v(S^v_m \rho^v - S^l_m \rho^l)) + \mu(\varepsilon_m - V^v(\rho^v - \rho^l)) + \sigma A \ , \tag{A.23}$$

from the vapor and liquid phases

$$P^v = T S^v_v + \mu \rho^v - U^v_v \ , \tag{A.24}$$

$$P^l = T S^l_v + \mu \rho^l - U^l_v \ , \tag{A.25}$$

and equation A.23, a equation containing the a surface term can be found,

$$\sigma A - V^v(P^v - P^l) = \varepsilon_u - T\varepsilon_s - \mu\varepsilon_m \ , \tag{A.26}$$

and the heat input Q can, thus, be rewritten as

$$Q = \sigma A - V^v(P^v - P^l) - TS^l_m\varepsilon_m + T\varepsilon_s \ , \tag{A.27}$$

and using the equilibrium conditions and equation A.9, the heat input can be simplified to

$$Q = A\frac{\sigma}{3} + TS^l_m\varepsilon_m + T\varepsilon_s \ . \tag{A.28}$$

Enthalpy is more commonly found in tables, not entropy, therefore the following relation $H = TS + \mu m$ is used to rewrite equation A.28 in terms of enthalpy, using

$$T\varepsilon_s - TS^l_m\varepsilon_m = \big(TS^s_s - TS^l_m\Gamma\big)A + V^b(T(S^v_m\rho^v - S^l_m\rho^l) + TS^l_m(\rho^v - \rho_l)) \ , \tag{A.29}$$

$$T\varepsilon_s - TS^l_m\varepsilon_m = \big(TS^s_s - TS^l_m\Gamma\big)A + V^b\rho^v\big(TS^v_m - TS^l_m\big) \ , \tag{A.30}$$

$$T\varepsilon_s - TS^l_m\varepsilon_m = \big(TS^s_s - TS^l_m\Gamma\big)A + V^b\rho^v\big(h^v_m - h^l_m\big) \ . \tag{A.31}$$

The heat input Q now becomes

$$Q = A\big(\frac{\sigma}{3} + TS^s_s - TS^l_m\Gamma\big) + V^b\rho^v\big(h^v_m - h^l_m\big) \ . \tag{A.32}$$

The final step is to replace the surface entropy with a measurable quantity, looking at the change

of energy of the surface,

$$dU^s = TdS^s + \sigma dA + \mu dm^s \ , \tag{A.33}$$

and integrating for a process where there is no interface in the initial state to a state where there is an interface and at constant T and P, this yields

$$U_2^s - U_1^s = T(S_2^s - S_1^s) + \sigma(A_2 - A_1) + \mu(m_2^s - m_1^s) \ , \tag{A.34}$$

$$U^s = TS^s + \sigma A + \mu m^s \ , \tag{A.35}$$

since equation A.35 is valid for any state, from the total derivative the following relation must be true, such that,

$$S^s dT + Ad\sigma + m^s d\mu = 0 \ , \tag{A.36}$$

$$d\sigma = -S_s^s dT - \Gamma d\mu \ , \tag{A.37}$$

similarly for each of the two phases individually,

$$dP^v = -S_v^v dT - \rho^v d\mu \ , \tag{A.38}$$

$$dP^l = -S_v^l dT - \rho^l d\mu \ , \tag{A.39}$$

$$d\mu = -\frac{1}{\rho^v - \rho^l} d(P^v - P^l) - \frac{(S_v^v - S_v^l)}{\rho^v - \rho^l} dT \ . \tag{A.40}$$

Equation A.40 is inserted into equation A.37 and for shorthand $d(P^v - P^l) = d(\Delta P)$, giving,

$$d\sigma = \frac{\Gamma}{\rho^v - \rho^l} d(\Delta P) + \left(\Gamma \frac{(S_v^v - S_v^l)}{\rho^v - \rho^l} - \frac{S^s}{A} \right) dT \ , \tag{A.41}$$

and finally,

$$-\frac{d\sigma}{dT}\bigg|_{\Delta P} + \frac{\Gamma}{\rho^v - \rho^l} \left(S_V^v - S_V^l \right) = S_s^s \ , \tag{A.42}$$

which can be used in equation A.32 to yield,

$$Q = A \left(\frac{\sigma}{3} + T \left(-\frac{d\sigma}{dT}\bigg|_{\Delta P} + \frac{\Gamma}{\rho^v - \rho^l} \left(S_v^v - S_v^l \right) \right) - T S_m^l \Gamma \right) + V^b \rho^v \left(h_m^v - h_m^l \right) \ . \tag{A.43}$$

Terms with Γ can be simplified into enthalpy, giving

$$Q = A \left(\frac{\sigma}{3} - T \frac{d\sigma}{dT}\bigg|_{\Delta P} + \frac{\Gamma \rho^v}{\rho^v - \rho^l} \left(h_m^v - h_m^l \right) \right) + V^b \rho^v \left(h_m^v - h_m^l \right) \ . \tag{A.44}$$

This is a complete form for the heat input to form a a bubble at equilibrium with its surroundings. There are few key notes to keep in mind. First, all quantities such as the pressure difference between vapor and liquid are not the standard saturated states, therefore to relate the vapor pressure to the saturation pressure, and keeping in mind that the chemical potentials are equal, the following

equation would need to be solved,

$$\frac{\partial \mu}{\partial p} = \frac{1}{\rho} \ , \tag{A.45}$$

$$\Rightarrow \int_{p_l}^{p_{sat}} \frac{dp^l}{\rho^l} = \int_{p_v}^{p_{sat}} \frac{dp^v}{\rho^v} \ . \tag{A.46}$$

Second, the surface density Γ as stated at the beginning is not a directly measurable quantity, but the heat input Q can be expanded in terms where to first order do not contain this surface density. To do so, equation A.41 is used, resulting in

$$d\sigma = \frac{\Gamma}{\rho^v - \rho^l} d(\Delta P) + \left(\Gamma \frac{(S_v^v - S_v^l)}{\rho^v - \rho^l} - \frac{S^s}{A} \right) dT \ , \tag{A.47}$$

$$d\sigma = \frac{\Gamma}{\rho^v - \rho^l} d(\Delta P) \text{ at constant T} \ . \tag{A.48}$$

When both sides are integrated a relation between σ and Γ is obtained,

$$\frac{2\sigma_0}{r_0} = \frac{2\sigma}{r} = p^v - p^l \ , \tag{A.49}$$

$$\sigma = \sigma_0 + \int_0^{p^v - p^l} \frac{\Gamma}{\rho^v - \rho^l} d(\Delta P) \ . \tag{A.50}$$

To first approximation, if the range of pressures satisfy the approximation $\Gamma/(\rho^v - \rho^l) \approx$ constant then,

$$\sigma = \sigma_0 \left(1 + \frac{2}{r_0} \frac{\Gamma}{\rho^v - \rho^l} \right) \ . \tag{A.51}$$

Q can now be rewritten to simplify error propagation as

$$Q = Q_0 + Q_1 \frac{\Gamma}{r_0(\rho^v - \rho^l)} \cdots . \tag{A.52}$$

Appendix B

Finite Differences and Integration

This appendix closely follows *Numerical Analysis*[31].

The idea of representation of a derivative for a computer, or in a numerical sense, can be done in a multitude of ways, finite differences will be the focus of this document as it is the simplest representation and this is the method used in this thesis to solve the coupled differential equations 3.30 and 3.36. Let us start by defining the differences of a function. Let's assume a function, f, has been evaluated at points x_0 through x_j, equally spaced, these values would be written as $f(x_0),\ \ldots,\ f(x_j)$. The shorthand notation $f_0 = f(x_0)$ will be used throughout. A difference is then the arithmetic difference between two consecutive function evaluations. There are three possibilities for one difference: it can either be a forward, backward or central difference. The name convention is with respect to the reference point. This can be summarized with operators that act

on the function evaluation at the reference point,

$$f_1 - f_0 = \Delta f_0 \ , \tag{B.1}$$

$$= \nabla f_1 \ , \tag{B.2}$$

$$= \delta f_{1/2} \ . \tag{B.3}$$

Where Δ, ∇ and δ are the forward, backward and central difference operators respectively. It is useful to define an extra operator, μ, which is the averaging operator,

$$\mu f_0 = \frac{1}{2}\left(f_{-1/2} + f_{1/2} \right) , \mu\delta f_0 = \delta\mu f_0 = \frac{1}{2}(\delta f_{\frac{1}{2}} + \delta f_{\frac{-1}{2}}) \ , \tag{B.4}$$

$$\mu\delta f_0 = \delta\mu f_0 = \frac{1}{2}(f_{-1} - f_1) \ . \tag{B.5}$$

Higher order operators from successive applications of operators also exist, for example,

$$\delta^2 f_j = \delta(\delta f_j) = \delta(f_{j-\frac{1}{2}} - f_{j+\frac{1}{2}}) = \delta f_{j-\frac{1}{2}} - \delta f_{j+\frac{1}{2}} = (f_{j-1} - f_j) - (f_j - f_{j+1}) = f_{j-1} - 2f_j + f_{j+1} \tag{B.6}$$

It is possible to make use of a progressing operator, which as the name implies can move forward or backwards through function evaluations,

$$Ef(x) = f(x + \delta x) \ , \tag{B.7}$$

$$Ef_j = f_{j+1} \ , \tag{B.8}$$

$$E^{-1} f(x) = f(x - \delta x) \ , \tag{B.9}$$

$$E^{-1} f_j = f_{j-1} \ . \tag{B.10}$$

It is to be noted that δ inside $f(x+\delta x)$ is not the operator, but the step in that variables direction. A differential operator, $D \equiv d/dx$, from a Taylor expansion can be related to the progression operator in the following manner,

$$f_1 = f(x_0 + \delta x) = e^{(\delta x)D} f_0 \ , \tag{B.11}$$

therefore,

$$E = e^{(\delta x)D} \ . \tag{B.12}$$

This is a powerful tool and that can be used to describe the difference operators, for example the forward difference operator, δ,

$$\Delta f(x) = f(x+\delta x) - f(x) = Ef(x) - f(x) \ , \tag{B.13}$$

$$\Delta f_0 = f_1 - f_0 = (E-1)f \ , \tag{B.14}$$

$$\Delta = E - 1 \ . \tag{B.15}$$

Similarly, there exist at least three other operators, the backward, central operators and averaging operators. When applied at a point these operators describe actions, for example, the backward difference, is the action of taking the difference between the function evaluation at the point and the previous function evaluation. The central operator is the difference between the half way points on both sides. Finally, the averaging operator is the average of the two half way points on both

sides. This can be summarized with with the following formulae,

$$\nabla f(x) = f(x) - f(x-\delta x) = (1-E^{-1})f(x)\ , \tag{B.16}$$

$$\nabla = 1 - E^{-1} = (E-1)/E\ , \tag{B.17}$$

$$\delta f(x) = f(x+\frac{1}{2}\delta x) - f(x-\frac{1}{2}\delta x)\ , \delta = E^{\frac{1}{2}} - E^{-\frac{1}{2}}\ , \tag{B.18}$$

$$\mu f(x) = \frac{1}{2}[f(x+\frac{1}{2}\delta x) + f(x-\frac{1}{2}\delta x)]\ . \tag{B.19}$$

$$\mu = \frac{1}{2}(E^{\frac{1}{2}} + E^{-\frac{1}{2}})\ . \tag{B.20}$$

These difference operators are linear, commutative and posse an inverse, for an arbitrary operator O these relation would be respectively,

$$O(f+g) = Of + Og\ , \tag{B.21}$$

$$O_1(O_2 f) - O_2(O_1 f) = 0\ , \tag{B.22}$$

$$O^{-1}(Of) = f\ . \tag{B.23}$$

It is to be noted that the inverse of the central difference, σ, the central sum:

$$\sigma = \left(E^{\frac{1}{2}} - E^{-\frac{1}{2}}\right)^{-1}\ , \tag{B.24}$$

$$\sigma = E^{\frac{1}{2}}/(E-1)\ , \tag{B.25}$$

is not always commutative with δ. Recalling equations B.18 and B.20 it is possible to relate the

central difference operator, δ, and the averaging operator, μ, to the differential operator

$$\delta = E^{\frac{1}{2}} - E^{-\frac{1}{2}} \,, \tag{B.26}$$

$$\mu = \frac{1}{2}\left[E^{\frac{1}{2}} + E^{-\frac{1}{2}}\right] \,, \tag{B.27}$$

$$E = e^{(\delta x)D} \,, \tag{B.28}$$

$$\delta = 2sinh\left(\frac{1}{2}(\delta x)D\right) \,, \tag{B.29}$$

$$\mu = cosh\left(\frac{1}{2}(\delta x)D\right) \,. \tag{B.30}$$

For brevity, it is useful to shorthand $(\delta x)D$ to one letter, U:

$$E = e^{U}, \quad \delta = 2sinh\left(\frac{1}{2}U\right), \quad \mu = cosh\left(\frac{1}{2}U\right) \,, \tag{B.31}$$

so that,

$$U = \left[\frac{(sinh^{-1}(\frac{1}{2}\delta))}{\frac{1}{2}\delta}\right]\delta \,. \tag{B.32}$$

Since $\delta f = Uf + O(\delta x)^3$, expanding this relation in powers of δ or U, δ^n or U^n can be regarded as a quantity of order $(\delta x)^n$. Derivatives can now be expressed as differences. The idea, from here, is to use the known relation $(\delta x)Df_j = (\delta x)\frac{\partial f_j}{\partial dx} = (\delta x)f'_j = Uf_j$. If the first derivative as a function of the central difference operator is required, the relation would be of the form

$$(\delta x)f'_j = \phi\,\delta f_j \,, \tag{B.33}$$

where ϕ is an operator of the desired form for the right hand side,

$$\phi = \frac{U}{\delta} \, . \tag{B.34}$$

Before continuing, it should be realized that the central difference operator requires evaluations at half intervals, it is more useful to then make use of the averaging operator to make use of known function evaluations. This would yield the following,

$$(\delta x) f'_j = \phi \mu \delta f_j \tag{B.35}$$

$$(\delta x) f'_j = \frac{U}{\mu \delta} \mu \delta f_j \tag{B.36}$$

$$U^n = \left[\mu^{-1} \left\{ \frac{\left(sinh^{-1} \frac{1}{2} \delta \right)}{\frac{1}{2} \delta} \right\}^n \right] \mu \delta^n \tag{B.37}$$

$$\frac{U}{\mu \delta} = 1 - \frac{1}{6}\delta^2 + \frac{1}{30}\delta^4 - \frac{1}{140}\delta^6 + \frac{1}{630}\delta^8 + O(\delta x)^{10} \, , \tag{B.38}$$

and finally,

$$(\delta x) f'_j = \left[\mu \delta - \frac{1}{6}\mu \delta^3 + \frac{1}{30}\mu \delta^5 - \frac{1}{140}\mu \delta^7 + \frac{1}{630}\mu \delta^9 + O(\delta x)^{10} \right] f_j \tag{B.39}$$

$$(\delta x) f'_j = \frac{1}{2} \left[(f_{j+1} - f_{j-1}) - \frac{1}{6}(\delta^2 f_{j+1} - \delta^2 f j - 1) + \frac{1}{30}(\delta^4 f_{j+1} - \delta^4 f j - 1) \right. \tag{B.40}$$

$$\left. - \frac{1}{140}(\delta^6 f_{j+1} - \delta^6 f j - 1) + \frac{1}{630}(\delta^8 f_{j+1} - \delta^8 f j - 1) + O(\delta x)^{10} \right] \, . \tag{B.41}$$

To summarize the idea of derivatives written as differences for all the operators

$$(\delta x)f'_j = \begin{cases} (\frac{U}{\Delta}) = [1 - \frac{\Delta}{2} + \frac{\Delta^2}{3}]\Delta f_j + O(\delta x^4) \\ (\frac{U}{\nabla}) = [1 + \frac{\nabla}{2} + \frac{\nabla^2}{3}]\nabla f_j + O(\delta x^4) \\ (\frac{U}{\mu\delta}) = \left[1 - \frac{1}{6}\delta^2 + \frac{1}{30}\delta^4 - \frac{1}{140}\delta^6 + \frac{1}{630}\delta^8\right]\mu\delta f_j + O(\delta x)^{10} \end{cases} \tag{B.42}$$

Now that finite difference schemes can be built, they can be used to solve a test differential equation. This will expose a crucial concept, stability. The concept of stability is introduced with a test problem because of the complexity of the Navier-Stokes equation and the heat equation described in section 3.2. Let's assume a simple differential equation of the form

$$\frac{du}{dt} = \lambda u \tag{B.43}$$

$$u(0) = u_0 \ . \tag{B.44}$$

The derivatives on the left hand side are replaced with any finite difference scheme. In this particular problem, the goal is to advance the solution using the initial value, therefore using central differences as shown previously with equation B.41 in functional value form, to second degree

$$u'_j = \frac{1}{2\delta x}\left(\frac{1}{6}u_{j-2} - \frac{4}{3}u_{j-1} + \frac{4}{3}u_{j+1} - \frac{1}{6}u_{j+2}\right) + O(\delta x)^4 = \lambda u_j \ . \tag{B.45}$$

This requires known values two steps ahead which is not possible. Using backward differences

yields instead

$$u'_j = \frac{1}{\delta x}\left(\frac{3}{2}u_j - \frac{5}{2}u_{j-1} + \frac{3}{2}u_{j-2} - \frac{1}{2}u_{j-3}\right) + O(\delta x)^4 = \lambda u_j \ . \tag{B.46}$$

In this case, during the progression, more and more terms are added. Unfortunately, this is not always desirable due to what is called stability. A stable numerical procedure will converge to the solution. The stability analysis is the key to all numerical procedures, but entire books can written on the subject and the reader should be aware of it.

In essence, when solving a differential equation, the process of integration is used to find the solution; therefore, it is of interest to find integration formulae to solve these equations. Integration is an infinite sum between to points and has the property of smoothing while differentiating has the property of amplifying abrupt changes in a function. That is why most differential equations are solved by integration. The simplest form of integration is the trapezium rule,

$$\int_{x_0}^{x_1} f dx = \frac{1}{2}(\delta x)(f_0 + f_1) \ . \tag{B.47}$$

A more precise formula can be written as

$$\int_{x_0}^{x_1} f dx = \frac{1}{2}(\delta x)(f_0 + f_1 + C_1) \ , \tag{B.48}$$

but it is also known that

$$\int_{x_0}^{x_1} f' dx = f_1 - f_0 \ , \tag{B.49}$$

$$\int_{x_0}^{x_1} f dx = \frac{2(E-1)}{U} f_0 \ , \tag{B.50}$$

$$f_1 + f_0 = (E+1) f_0 \ , \tag{B.51}$$

therefore

$$C_1 = \left[\frac{2(E-1)}{U} - (E+1) \right] f_0 \ . \tag{B.52}$$

Different integration formulae are given by different ways of expressing C. There a special class of methods called the Runge-Kutta methods. These methods are one step in the sense they only require one value. In essence, the method is the use of a weighted sum of of the slope at four points along the integration step. To have some kind of a point of reference the "Simpson's Rule" will be derived and used as comparison. In the previous development, integration was performed over one step but if integration is performed over multiple steps it would yield

$$\int_{x_{-k}}^{x_k} f dx = \left(\frac{2(E^k - E^{-k})}{U} \right) f_0 \ , \tag{B.53}$$

$$\int_{x_{-k}}^{x_k} f dx = \left(\frac{2(sinh(kU))}{U} \right) f_0 \ . \tag{B.54}$$

To first approximation this is $2k(\delta x) f_0$, therefore the correct operator to expand would be $\frac{2(sinh(kU))}{kU}$ which would give,

$$\int_{x_{-k}}^{x_k} f dx = 2(\delta x)[f_0 + \frac{1}{6}\delta^2 f_0 - \frac{1}{180}\delta^4 f_0 + \frac{1}{1512}\delta^6 f_0] + O(\delta x^9) \ , \tag{B.55}$$

the first two terms are what are referred to as the "Simpson's rule". When expressed in term of function values,

$$\int_{x_{-k}}^{x_k} f dx = 2(\delta x)[f_0 + \frac{1}{6}(f_1 - 2f_0 + f_{-1})] = \frac{1}{3}(\delta x)[f_1 + 4f_0 + f_{-1}] \ . \tag{B.56}$$

In this particular case δx is an integer, but nothing disallows taking half steps and starting at x_0 in which case the expression would be

$$\int_{x_0}^{x_1} f dx = \frac{1}{6}(\delta x)[f_1 + 4f_{\frac{1}{2}} + f_0] \ . \tag{B.57}$$

Returning to the test differential equation, the formulae developed previously can still be used by replacing $f \to f'$. Runge-Kutta uses the idea of estimating the slope twice at the mid-point to give

$$\int_{x_0}^{x_1} f' dx = f_1 - f_0 = \frac{1}{6}(\delta x)[f'_1 + 2f'^1_{\frac{1}{2}} + 2f'^2_{\frac{1}{2}} + f'_0] \ . \tag{B.58}$$

The superscripts for the derivative at mid point is only an indication that they are both different from that of Simpson's rule. To get to equation B.58, the first slope is calculated as follows,

$$f'_0 = \lambda f_0 \ , \tag{B.59}$$

if the midpoint is calculated,

$$f^*_{\frac{1}{2}} = f_0 + \frac{(\delta x)}{2} f'_0 \ , \tag{B.60}$$

since this midpoint is an approximation a "*" superscript is added. To continue, the slope is re-

evaluated at this point,

$$f'^{1}_{\frac{1}{2}} = \lambda f^{*}_{\frac{1}{2}} \,, \tag{B.61}$$

A new midpoint is re-calculated using this slope,

$$f^{**}_{\frac{1}{2}} = f_0 + \frac{(\delta x)}{2} f'^{1}_{\frac{1}{2}} \,, \tag{B.62}$$

Again a new slope at midpoint is calculated

$$f'^{2}_{\frac{1}{2}} = \lambda f^{**}_{\frac{1}{2}} \,, \tag{B.63}$$

this is used to find an approximated end-point,

$$f^{*}_{1} = f_0 + (\delta x) f'^{2}_{\frac{1}{2}} \,, \tag{B.64}$$

a final slope is found,

$$f'_1 = \lambda f^{*}_{1} \,. \tag{B.65}$$

To progress the solution to the end-point a weighted sum of all the slopes is used,

$$f_1 = f_0 + \frac{1}{6}(\delta x)[f'_1 + 2f'^{1}_{\frac{1}{2}} + 2f'^{2}_{\frac{1}{2}} + f'_0] \,. \tag{B.66}$$

It should be noted that uncertainties have not been discussed in this appendix due to the difficulty of analyzing the uncertainties of a particular numerical method. However, the study of uncertainties, including both local and global errors, is crucial to any numerical method. It is assumed *a priori*

that the chosen method is stable and errors do not grow and diverge.

Bibliography

[1] F. Zwicky, *On The Masses of Nebulae and of Clusters of Nebulae*, The Astrophysical Journal, Vol. 86, Num. 3, pp. 217-246 (1937).

[2] F. Zwicky, *On the Red Shift of Spectral Lines Through Interstellar Space*, Proc. N. A. S., Vol. 15, pp.773-779 (1929).

[3] Vera C. Rubin and W. Kent Ford Jr., *Rotation of Andromeda Nebula From a Spectroscopic Survey of Emission Regions*, The Astrophysical Journal, Vol. 159, pp. 379-403 (1970).

[4] V. C. Rubin and S. D'Odorico, *A Note on the Systemic Velocity of M 31*, Astron. & Astrophys. 2, pp. 484-488 (1969).

[5] Amole C. et. al., *Dark Matter Search Results from the PICO-60 C_3F_8 Bubble Chamber*, Phys. Rev. lett. 118 (2017).

[6] H. Arp, *Spiral Structure in M31*, Ap. J., vol. 139, p.1045 (1964).

[7] F. Simien et al., *The Spiral Structure of M31: A Morphological Approach*, Astron. Astrophys., vol. 67,pp.73-79 (1978).

[8] V. Zacek, *Dark Matter*, arXiv:0707.0472 (2007).

[9] S.Y.F. Chu, et al., *The Lund/LBNL Nuclear Data Search*, http://nucleardata.nuclear.lu.se/toi/ (1999).

[10] P. R. Bevington, D. K. Robinson, *Data Reduction and Error Analysis*, mcGraw Hill Higher Education, Third Edition (2003).

[11] D. Griffiths, *Introduction to Elementary Particles*, Wiley-VCH (2004).

[12] C. Patrignani et al. (Particle Data Group), Chin. Phys. C, 40, pp. 510 (2016 and 2017 update).

[13] S. Agostinelli et. al., *Geant4-aSimulation Toolkit*, Nuclear instruments and methods, Vol. 506, Issue 3, pp. 250-303 (2003).

[14] J. D. Lewin,P. F. Smith, *Review of Mathematics, Numerical Factors, and Corrections for Dark Matter Experiments Based on Elastic Nuclear Recoil*, Astroparticle Physics 6, Elsivier (1996).

[15] U.S. Department of Defense, Military Standard: Products Cleanliness Levels and Contamination Control Program (1994).

[16] E. Behnke et al., *First dark matter search results from a 4-kg CF_3I bubble chamber operated in a deep underground site*, Phys. Rev. D 86 (2012).

[17] Hu Seung Lee and Herman Merte, *Spherical Vapor Bubble Growth in Uniformly Superheated Liquids*, International Journal of Heat and Mass Transfer, Vol. 39, No12, pp. 2427-2447 (1995).

[18] Bloch F., Ann. Physik, Vol. 16, pp. 285-320 (1933); Bloch F., Zeit. Phys., Vol. 81, pp. 363-376 (1933).

[19] Anthony J. Robinson, *Bubble Growth Dynamics in Boiling*, Ph. D. thesis, McMaster University (2002).

[20] Kajishima T. and Taira K., *Computational Fluid Dynamics Incompressible Turbulent Flows*, Springer (2017).

[21] Wendt J., *Computational Fluid Dynamics an Introduction*, Springer (2009).

[22] T. G. Leighton, *The Acoustic Bubble*, Academic Press (1997).

[23] J. F. Ziegler, M.D. Ziegler, J.P. Biersack, *SRIM – The Stopping and Range of Ions in Matter (2010)*, Nucl. Inst. Methods, B268, 1818-1823 (2010)

[24] J. F. Ziegler, J. P. Biersack and M. D. Ziegler, *SRIM - The Stopping and Range of Ions in Matter*, LuLu Press (2008).

[25] G. Fontaine, *Compléments de Mécanique Statistique*, Université de Montréal, manuscript.

[26] C. E. Dahl, J. Hall and W. H. Lippincott, *Things That Go Plink in a Bubble Chamber*, Internal document PICO collaboration.

[27] C. E. Dahl, *Seitz Model Revisited*, Internal document PICO collaboration.

[28] Iran N. Levine, *Physical Chemistry*, McGraw-Hill (1995).

[29] Arthur W. Adamson, *A Textbook of Physical Chemistry*, Academic Press (1979).

[30] J. Willard Gibbs, *On the Equilibrium of Heterogeneous Substances*, Tuttle, Morehouse & Taylor, Printers, New Haven pp.108-248 (1874-1878).

[31] D. R. Hartree, *Numerical Analysis*, Oxford university Press (1958).

[32] Susan M. Lea, *Mathematical Tools for Physicists*, Brooks/Cole-Thomson (2003).

[33] S. Plimpton, *Fast Parallel Algorithms for Short-Range Molecular Dynamics*, J Comp Phys, 117, pp.1-19 (1995)

[34] Marcus D Hanwell et. al., *Avogadro: An advanced semantic chemical editor, visualization, and analysis platform*, Journal of Cheminformatics, pp.4:17 (2012).

[35] E.W. Lemmon, I. H. Bell, M. L. Huber, M. O. McLinden, *NIST Standard Reference Database 23: Reference Fluid Thermodynamic and Transport Properties-REFPROP*, Version 10.0, National Institute of Standards and Technology, Standard Reference Data Program, Gaithersburg (2018).